CrossMark
← click for updates

# Novel Approaches Reveal that *Toxoplasma gondii* Bradyzoites within Tissue Cysts Are Dynamic and Replicating Entities *In Vivo*

Elizabeth Watts,[a]* Yihua Zhao,[b] Animesh Dhara,[a] Becca Eller,[a]* Abhijit Patwardhan,[b] Anthony P. Sinai[a]

Department of Microbiology, Immunology and Molecular Genetics, University of Kentucky College of Medicine, Lexington, Kentucky, USA[a]; Department of Biomedical Engineering, University of Kentucky College of Engineering, Lexington, Kentucky, USA[b]

* Present address: Elizabeth Watts, Coverdell Center for Biomedical and Health Sciences, University of Georgia, Athens, Georgia, USA; Becca Eller, Nestle, USA, Mt. Sterling, Kentucky, USA.

**ABSTRACT** Despite their critical role in chronic toxoplasmosis, the biology of *Toxoplasma gondii* bradyzoites is poorly understood. In an attempt to address this gap, we optimized approaches to purify tissue cysts and analyzed the replicative potential of bradyzoites within these cysts. In order to quantify individual bradyzoites within tissue cysts, we have developed imaging software, BradyCount 1.0, that allows the rapid establishment of bradyzoite burdens within imaged optical sections of purified tissue cysts. While in general larger tissue cysts contain more bradyzoites, their relative "occupancy" was typically lower than that of smaller cysts, resulting in a lower packing density. The packing density permits a direct measure of how bradyzoites develop within cysts, allowing for comparisons across progression of the chronic phase. In order to capture bradyzoite endodyogeny, we exploited the differential intensity of TgIMC3, an inner membrane complex protein that intensely labels newly formed/forming daughters within bradyzoites and decays over time in the absence of further division. To our surprise, we were able to capture not only sporadic and asynchronous division but also synchronous replication of all bradyzoites within mature tissue cysts. Furthermore, the time-dependent decay of TgIMC3 intensity was exploited to gain insights into the temporal patterns of bradyzoite replication *in vivo*. Despite the fact that bradyzoites are considered replicatively dormant, we find evidence for cyclical, episodic bradyzoite growth within tissue cysts *in vivo*. These findings directly challenge the prevailing notion of bradyzoites as dormant nonreplicative entities in chronic toxoplasmosis and have implications on our understanding of this enigmatic and clinically important life cycle stage.

**IMPORTANCE** The protozoan *Toxoplasma gondii* establishes a lifelong chronic infection mediated by the bradyzoite form of the parasite within tissue cysts. Technical challenges have limited even the most basic studies on bradyzoites and the tissue cysts *in vivo*. Bradyzoites, which are viewed as dormant, poorly replicating or nonreplicating entities, were found to be surprisingly active, exhibiting not only the capacity for growth but also previously unrecognized patterns of replication that point to their being considerably more dynamic than previously imagined. These newly revealed properties force us to reexamine the most basic questions regarding bradyzoite biology and the progression of the chronic phase of toxoplasmosis. By developing new tools and approaches to study the chronic phase at the level of bradyzoites, we expose new avenues to tackle both drug development and a better understanding of events that may lead to reactivated symptomatic disease.

Address correspondence to Anthony P. Sinai, sinai@uky.edu.

*Toxoplasma gondii*, an important opportunistic infection in HIV-AIDS is transmissible by two distinct cyst forms, the oocyst shed in cat feces at the end of the sexual cycle and the tissue cyst formed in all vertebrate hosts in the course of the asexual cycle in the intermediate host (1). In humans and other warm-blooded animals, infection acquired by either the ingestion of the environmental oocysts or the ingestion of tissue cysts in the act of carnivory manifests, and an acute infection associated with the rapid replication and spread within the body of the tachyzoite forms (1, 2). This phase of infection is most often asymptomatic, as the infection is readily controlled by the immune system. However, unlike other infections, a sterile cure is not achieved, as the parasite differentiates into a slowly growing bradyzoite, establishing itself within tissue cysts primarily in the central nervous system (CNS) and muscle (1, 3). These tissue cysts are maintained for the life of the host, progressing in their cycle during carnivory, completing the cycle when the carnivore is a feline (1, 4).

Tissue cysts in the host are kept under control by the immune system and are believed to undergo cycles of reactivation (to tachyzoites) and redifferentiation back to bradyzoite-containing cysts (5, 6). In the absence of immune function, most notably the loss of T-cell immunity, such as that seen in active HIV-AIDS, tissue cyst reactivation occurs, but given the lack of immune function in the host, tachyzoite replication continues unchecked (7).

Untreated active toxoplasmosis typically manifesting as toxoplasmic encephalitis is lethal in the context of active HIV-AIDS (8). Given the high seroprevalence of *Toxoplasma* infections in the general human population that approaches 30% worldwide (9) and the life-long persistence of the agent within tissue cysts presents this poorly understood life cycle form as the primary source of symptomatic toxoplasmosis in the HIV-AIDS populations (8).

Much of what we know about bradyzoite biology comes from a combination of detailed and classic morphological studies (3, 10–14) as well as cell culture-based systems (15–17). The electron microscopic studies provide distinct features of bradyzoites, including a more posterior location of the nucleus, altered features of the rhoptries which appear less mottled than the tachyzoite organelles, and the presence of starch storage (amylopectin) granules within the organisms (10–12). The bradyzoites themselves are arranged in no specific orientation (unlike the rosettes of tachyzoites) within the tissue cyst (11, 12) that itself is delimited by a thick glycan-rich cyst wall that appears to be assembled under the erstwhile parasitophorous vacuole membrane (PVM) (18–21). Another notable feature of the organization within the tissue cyst is the presence of a matrix of mildly osmophilic material between bradyzoites (11, 12, 21). The number of bradyzoites within the tissue cyst has not been measured in part due to the random orientation of the organisms and their sheer number, which varies with differences in cyst size. Accordingly, tissue cyst sizes *in vivo* have been estimated to range from 25 to 70 $\mu$m in diameter with few cysts outside this range (3, 11, 12). Here again, the relatively low incidence of cysts in brain sections has limited the determination of the cyst burden to estimates, although some estimates have been made using this approach (11, 12). Finally, there has not been a means of establishing the true bradyzoite burden within tissue cysts, a value that is crucial to establish the potential effects of immune parameters and drugs.

Cell culture-based systems to trigger tachyzoite differentiation to bradyzoites within *in vitro* tissue cysts have been useful in establishing the basic framework for the functional understanding of bradyzoite biology (15–17, 22). On the basis of these studies, a diverse range of physical and pharmacological stressors have been shown to trigger stage conversion based on limited criteria to define bradyzoites and tissue cysts (reviewed in references 23 and 24). These criteria include the conversion of the poorly glycosylated PVM into an extensively glycosylated cyst wall detected using lectins, primarily *Dolichos biflorus* agglutinin (DBA) lectin (18, 25, 26), the selective induction of bradyzoite-specific markers (such as TgSRS9 [*T. gondii* SRS9] (27, 28) and TgBAG1 [*T. gondii* BAG1] (29)) accompanied by the downregulation of the tachyzoite-specific TgSAG1 (*T. gondii* surface antigen 1) (28, 30). In addition, consistent with a reduction in the overall growth rate and metabolic function, key enzymes in intermediary metabolism, including components of the glycolytic pathway (lactate dehydrogenase [31, 32] and enolase [32–34]) experience a shift in the isoforms being expressed (23, 24). Not surprisingly, these changes in gene expression occur on a global level consistent with the reprogramming of the organisms for the chronic "nonreplicative" phase of the developmental cycle (23, 24, 35). The recent discovery of the AP2 family of transcription factors, several of which are key regulators of stage conversion (17, 22, 36) and the effects of epigenetic phenomena support the notion that a highly regulated series of events underlies bradyzoite conversion and cyst formation (23, 37, 38).

Despite all the progress made by investigating bradyzoite conversion and tissue cyst biology in cell culture, we know little to nothing about what occurs *in vivo*. Direct extrapolation of cell culture-derived results to the *in vivo* context, while appropriate to a degree, does not begin to address the true *in vivo* situation. As a result, the actual triggers for stage conversion, replicative capacity of bradyzoites within cysts, patterns of potential replication within cysts, and dynamics of cyst populations during the course of establishment and entrenchment of the chronic phase of *Toxoplasma* infection remain unknown. Detailed biochemical and cell biological analyses have been limited by the difficulties inherent in the generation of cysts in numbers conducive to such analyses. In this study, we focused on the optimization and standardization of the tissue cyst generation and purification protocol to provide for the first time tissue cysts in numbers that are conducive to cell biological interrogation.

A fundamental conceptual impediment to our understanding of bradyzoite dynamics has been a mindset that posits that all tissue cysts and therefore bradyzoites are equivalent. This narrow mindset has been entrenched largely due to the absence of markers to discriminate the potential diversity of physiological states for bradyzoites within a tissue cyst. The classic markers, including lectin reactivity (DBA) (18, 25, 26), upregulation of "bradyzoite-specific" markers (BAG1/5, ENO1, and BradySAGs) and the downregulation of tachyzoite-specific genes, such as SAG1, ENO2, and nucleoside triphosphate hydrolase (NTPase), are excellent indicators of the transition to cysts (16, 28–34, 39, 40) but are largely uninformative with regard to the physiological status of any given bradyzoite or of differences between them. The focus on the "tissue cyst," rather than the bradyzoite, has been driven by the inability to monitor individual bradyzoites within tissue cysts, thereby preventing the collection of data on the level of individual parasites. We therefore sought to develop new approaches to overcome this major barrier to understanding the dynamics of the organisms within tissue cysts that can be very informative in the context of both the basic biology and drug development.

Our studies reveal a remarkable level of heterogeneity in tissue cyst organization and function. Most notably, our data directly challenge the notion that bradyzoites within tissue cysts are dormant and lack replication potential. Rather, we find compelling evidence that bradyzoites are considerably more dynamic than previously imagined and that they exhibit patterns of growth and development that have not been appreciated. We not only capture direct evidence for bradyzoite replication within tissue cysts but also gain insights into the patterns of replication in the context of the progression of the chronic phase *in vivo*. These approaches promise to revolutionize our understanding of this enigmatic life cycle stage of *Toxoplasma gondii* and will provide new insights into the development of new drugs by providing a framework within which antibradyzoite (rather than anti-tissue cyst) activities can be quantified and evaluated in the context of infection *in vivo*.

## RESULTS

**The optimization of tissue cyst purification exposes temporal changes in their physical properties.** A significant limitation to the cell biological and biochemical study of tissue cysts has been the lack of standardization of methods to purify *in vivo* cysts from the central nervous system (CNS). We therefore focused on refining the original Percoll gradient purification system developed by Cornelissen et al., which employed a continuous-density gradient

formed by layering the cyst-containing brain homogenate on 30% Percoll, itself formed on a 90% Percoll cushion (41). In this gradient system, murine erythrocytes collect as a distinct band at the 30%/90% interface, with tissue cysts concentrating right above this layer (41). While the red blood cell (RBC) layer provides a convenient internal marker, the comingling of cysts with this layer results in cyst fractions that are substantially contaminated with erythrocytes (data not shown). Furthermore, the concentration of cysts within this narrow band precludes the resolution of potentially subtle differences in density that report on the overall lipid/nonlipid ratio of cysts at equilibrium density.

In order to expand the resolution range of the collection layer (between the RBC band and the bulk brain homogenate) (Fig. 1A), we tested several gradient configurations. The optimal configuration was found to retain the 90% Percoll cushion (9 ml) overlaid with a discontinuous gradient of 40% Percoll (4.5 ml) and 20% Percoll (4.5 ml) on which the brain homogenate was layered prior to centrifugation (Fig. 1A; see Text S1 in the supplemental material). Following centrifugation, the tissue cysts were found to be distributed across the region bounded by the RBC layer and the brain homogenate (Fig. 1A). The gradients were harvested in roughly 1-ml fractions by carefully inserting a glass capillary into the bottom of the gradient and pumping the gradient out using a peristaltic pump (Fig. 1A). Quantification of tissue cyst numbers in gradient fractions was established by direct enumeration on an inverted tissue culture microscope following the transfer of 10 $\mu$l of each fraction into the wells of a 96-well plate containing 100 $\mu$l of phosphate-buffered saline (PBS) and pelleting (Text S1). Imaging of tissue cysts was achieved by centrifuging cysts onto slides using a Cytospin centrifuge and subsequent staining as indicated below in Materials and Methods. Purified tissue cysts were found for the most part to be resilient, emerging intact following the homogenization, syringe passages, and resolution on the gradients. We did, however, find that very immature tissue cysts, defined by thin cyst walls, as well as some of the largest cysts were fragile (examples given below). The potential selective loss of cysts during purification could impact the absolute numbers purified but are not expected to alter the overall pattern of purified cysts over time.

The standardization of the Percoll gradient method allows for the direct assessment of tissue cyst distribution on the basis of their density. Therefore, we used Percoll calibration beads (Cospheric, Santa Barbara, CA) to establish the mean density of individual fractions. A representative gradient alongside a gradient run using the calibration beads reveals that a largely linear gradient is formed between the 90% cushion and the brain homogenate (see Fig. S1 in the supplemental material). We compiled data for the cyst density distribution accumulated over roughly 2 years (a total of 99 gradients) for animals infected for 3 weeks (days 21 to 27), 4 weeks (days 28 to 34), 5 weeks (days 35 to 41), 6 weeks (days 42 to 48), and 8 weeks (days 56 to 63) to determine whether any patterns related to their physical properties across this time range would emerge. For all time points, the majority of tissue cysts sediment to fractions 14 to 16, where the computed Percoll density is between 1.055 and 1.040 mg/ml³ (Fig. 1B and Fig. S1). Purified tissue cysts were predominantly spherical, with a small fraction (<5%) appearing ovoid, consistent with earlier findings (42). Closer examination of cysts using Nomarski illumination (differential interference contrast [DIC]) however showed subtle but consistent differences in the "texture" of tissue cysts as a func-

tion of the duration of infection (Fig. 1B). These differences manifest with regard to the delineation of the resident bradyzoites that tend to be more clearly demarcated earlier in the chronic phase rather than later (Fig. 1B). The distribution of cysts within the gradients as a function of the duration of infection was found to vary, as evident from the area under the curve from fractions 10 to 13 (high-density cysts), 14 to 16 (intermediate-density cysts [peak fractions]), and 17 to 19 (low-density cysts) (Fig. 1C). Paradoxically, the proportion of high-density tissue cysts is highest early in the chronic phase (week 3 to 4) and decreased with increasing time of infection, resulting in tissue cysts harvested at weeks 6 and 8 tending to have more low-density cysts than observed at earlier time points (Fig. 1C). Together, these data reveal that tissue cysts are not likely to be static entities, as their relative density changes with the progression of the chronic phase.

**The mean tissue cyst burden, while heterogenous, exhibits a similar relative temporal distribution.** The cyst burdens in the brains of mice infected for 3, 4, 5, 6, and 8 weeks using an intraperitoneal (i.p.) injection of 18 to 20 tissue cysts in brain homogenate as the inoculum were established following the purification on Percoll gradients as described above (Fig. 2A). For all time points, the number of cysts per brain (total number per gradient divided by 2, see the purification protocol in Text S1 in the supplemental material) was not found to be statistically different despite considerable heterogeneity at each time point (Fig. 2A and Table 1). The greatest heterogeneity in purified cyst numbers was observed for the earlier time points and was found to be remarkably consistent and stable as the chronic phase progressed, suggesting the establishment of an equilibrium (Fig. 2A). The tissue cyst yields and inherent variability were consistent with the values estimated from counting cysts in brain sections using *T. gondii* ME49 parasites in CBA/CA mice (43).

Tissue cysts in the brain are initially established by the conversion of tachyzoites to bradyzoites (reviewed in reference 23). Following the establishment of immunity and the clearance of tachyzoites, the formation of new cysts from the primary acute infection is believed to cease on account of the clearance of the tachyzoites (44). This is consistent with the tissue cyst burden remaining stable rather than increasing over time in the absence of reactivation (Fig. 2A). In reality, reactivation, which can result in the reseeding of new cysts as the chronic phase progresses, does occur, although this is a rare event (45). We appear to have captured just such a reseeding event within a brain section where both *Dolichos* lectin (DBA)-positive tissue cysts and DBA-negative tachyzoite vacuoles are found in close proximity 4 weeks postinfection (Fig. 2B). Reactivation of tissue cysts would be expected to release several hundreds of parasites (see below). If a substantial proportion of these parasites reestablished new cysts, we would predict an increase in the total number of cysts over time. This is not observed (Fig. 2A and Table 1). Rather, the loss of a tissue cyst and the hundreds of parasites within it appears to establish on average a single viable cyst, resulting in a general equilibrium in the cyst burden over the time frame examined (Fig. 2A and Table 1). This would indicate that in the presence of a competent immune system, parasites released from cysts are efficiently cleared as noted previously (45).

**Tissue cysts grow in size during the course of chronic infection.** Tachyzoite-to-bradyzoite conversion is tightly regulated (17, 23, 36), although the exact natural triggers remain elusive. Studies of cell culture systems indicate that the commitment to differen-
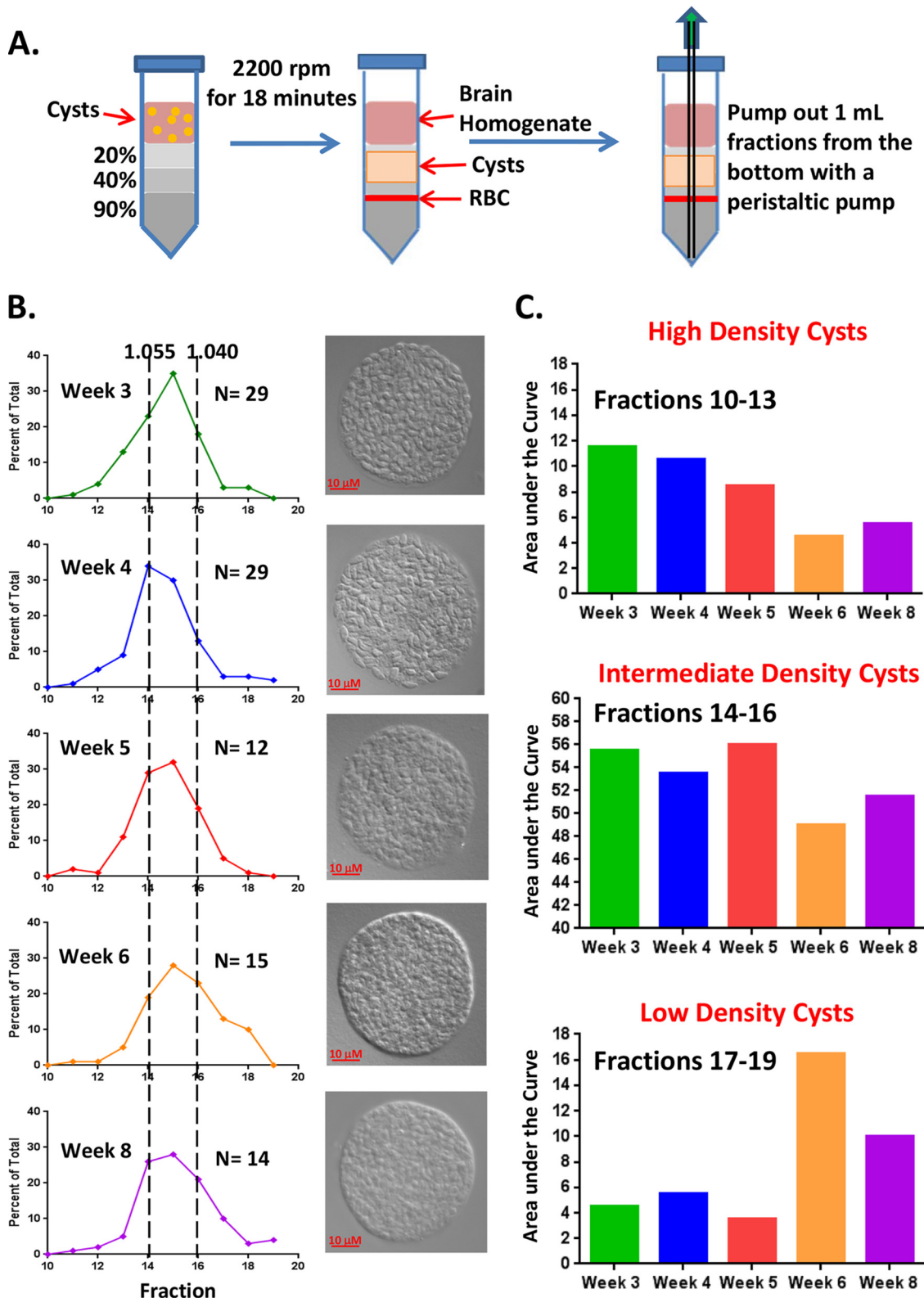
FIG 1 Tissue cyst purification using modified Percoll gradients. (A) Schematic setup of a three-step Percoll gradient containing 90%, 40%, and 20% Percoll overlaid with brain homogenate containing tissue cysts. The tissue cysts resolve between the 90%/40% Percoll interface above the host RBC and below the bulk brain homogenate, which was layered onto the 20% Percoll layer. Tissue cysts are harvested as roughly 1-ml fractions from the bottom of the gradient to the interface between the 20% Percoll and the brain homogenate. (B) Distribution of tissue cysts in the gradients (fractions 10 to 19) relative to the time of harvest postinfection. The bulk of tissue cysts for all times of harvest are of an intermediate density (1.055 and 1.040 mg/ml$^3$). However, the relative proportions of high-density ($>$1.055 mg/ml$^3$) and low-density ($<$1.040 mg/ml$^3$) cysts exhibit a shift toward less-dense cysts over time. Nomarski (DIC) images of representative

*(Continued)*
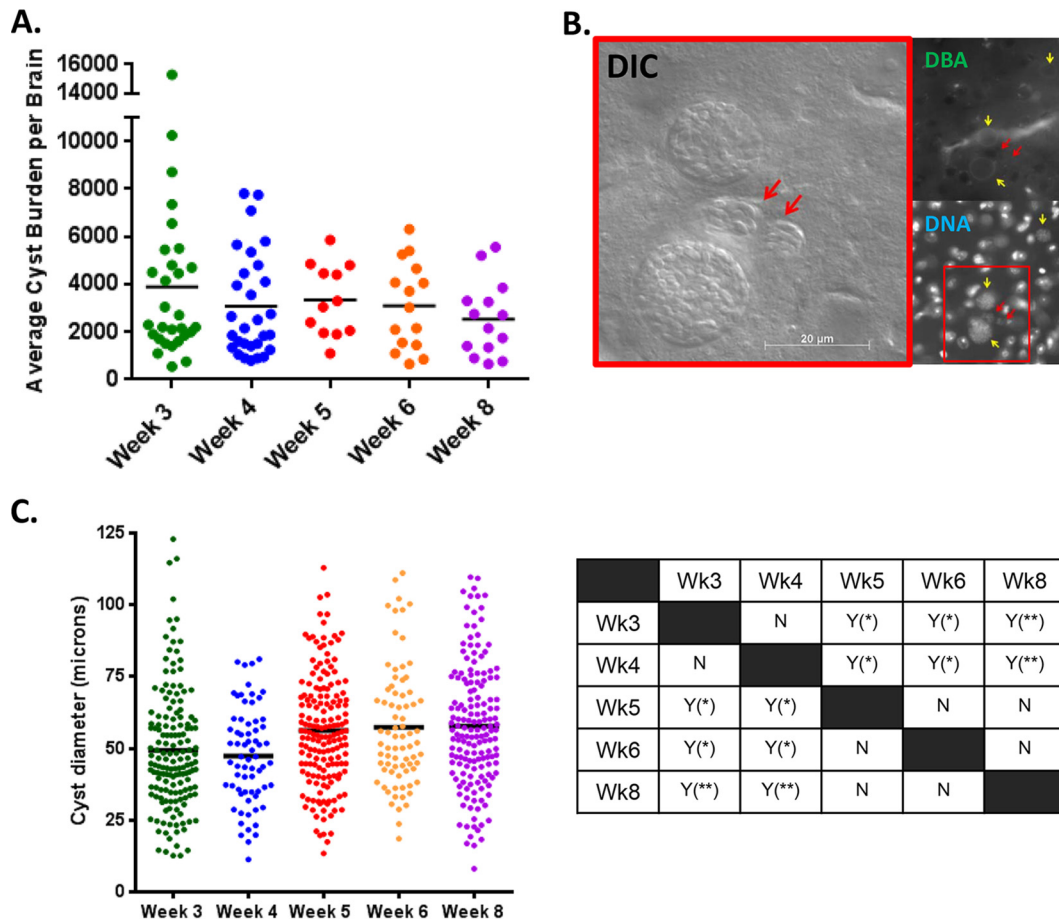
FIG 2 Tissue cyst yields and size distribution during the course of chronic infection. (A) The average tissue cyst yield from 99 independent Percoll gradient purifications was established as described in Materials and Methods. In spite of considerable heterogeneity at each time point, the mean yield (black line) was found to be very similar and not statistically significant (one-way ANOVA, $F_{4,94} = 0.8892$ [$P = 0.4736$], $\alpha = 0.05$). The mean tissue cyst burden per mouse was established as described in Materials and Methods and in Text S1 in the supplemental material. The actual means and standard deviations are reported in Table 1. (B) Evidence of spontaneous reactivation in the brain of an infected CBA/J mouse harvested 4 weeks postinfection. The enlarged DIC image reveals two tissue cysts and two tachyzoite vacuoles (red arrows). The tissue cysts are evident as *Dolichos biflorus* agglutinin (DBA) lectin-positive halos and by the patterns of the DNA labeling (small yellow arrows). In contrast, the tachyzoites vacuoles lack a cyst wall, and as a result, they are DBA negative (small red arrows). (C) Distribution of the diameters of tissue cysts harvested 3, 4, 5, 6, and 8 weeks postinfection exhibit considerable heterogeneity at all time points. Statistical analysis by ANOVA reveals diverse level of significance ($F_{4,625} = 6.307$; $P < 0.0001$). The analysis between weeks was done using Tukey's pairwise multiple-comparison test ($\alpha = 0.05$). A mean diameter (black line) that differed significantly from another is indicated by the letter Y (for yes), and the level of significance is indicated by the number of asterisks. The letter N (for no) indicates that the two mean diameters being compared did not differ significantly.

tiate can be initiated in tachyzoite vacuoles of different sizes bearing different numbers of parasites (15, 16, 39, 46, 47). This heterogeneity in the vacuolar size at the time of differentiation is a likely contributing factor to the heterogeneity in the size of newly formed tissue cysts that is evident even in the week 3 tissue cysts (Fig. 2C). Tissue cysts are viewed as being metabolically inert, containing nonreplicative or slowly replicating bradyzoites (24). If this were true, the primary determinant of tissue cyst diameter (volume) would be the size at the time of inception (stage conversion), which should then remain largely fixed. Morphometric

analysis from brain sections, however, suggests that tissue cysts increase in size over time, a property suggested to be linked to bradyzoite replication (12, 43). We measured the diameters of randomly acquired purified tissue cysts at all time points of harvest using the AxioVision morphometric suite calibrated using a stage micrometer (Zeiss). The mean tissue cyst diameter for all measured cysts was found to be 54.1 $\mu$m with a standard deviation of 20.6 $\mu$m (Fig. 2C and Table 1). Analysis of the distribution of tissue cyst diameters for cyst populations at different infection times was found to be relatively consistent with modest statistical

*Figure Legend Continued*

tissue cysts (all between 50 and 52 $\mu$m in diameter) exhibit increased loss of demarcation of bradyzoites as a function of the time of infection. (C) The relative distribution of tissue cysts as a function of time of infection represented as the area under the curve for high-density cysts (>1.055 mg/ml³), intermediate-density cysts (1.055 to 1.040 mg/ml³), and low-density cysts (<1.040 mg/ml³) exhibits a time-dependent reduction of high-density tissue cysts and increasing low-density cysts as a function of the time of harvest. These data are a compilation of 99 independent gradients with the number of gradients harvested at each time point indicated in the distribution curves in panel B.

**TABLE 1** Number and size distribution of tissue cysts over the course of infection

| Time point (wk) | No. of gradients | Cyst yield (mean no. of cysts [SD]) | Diameter ($\mu$m) (mean [SD]) | No. (%) of cysts with the following diameter: | | | Total no. of cysts |
|---|---|---|---|---|---|---|---|
| | | | | <40 $\mu$m | 40 to 70 $\mu$m | >70 $\mu$m | |
| 3 | 29 | 3888 (3268) | 49.3 (21.1) | 51 (33) | 81 (52) | 24 (15) | 156 |
| 4 | 29 | 3072 (2170) | 47.3 (16.8) | 23 (34) | 40 (59) | 5 (7) | 68 |
| 5 | 12 | 3342 (1499) | 56.2 (19.4) | 33 (20) | 98 (58) | 38 (22) | 169 |
| 6 | 15 | 3086 (1829) | 57.4 (21.1) | 15 (20) | 43 (56) | 18 (24) | 76 |
| 8 | 14 | 2540 (1567) | 57.7 (21.5) | 32 (20) | 85 (53) | 44 (27) | 161 |
| Total | 99 | 3271 (2379) | 54.1 (20.6) | 154 (24) | 347 (55) | 129 (21) | 630 |

differences evident in the pairwise analysis (Fig. 2C). These modest differences in the size distribution of tissue cysts suggest that tissue cyst size is impacted primarily by vacuolar size at the time of stage conversion and to a lesser extent by cyst growth after conversion.

Although pairwise analysis reveals modest statistical differences when examining the entire population of cysts, more meaningful insights are gained from the examination of the temporal distributions of what we arbitrarily classify as small (<40-$\mu$m-diameter), intermediate (40- to 70-$\mu$m-diameter), and large (>70-$\mu$m-diameter) cysts. The temporal pattern clearly indicates a marked drop in the percentage of small cysts between the early (week 3 to 4) and later (week 5 to 8) time points (Table 1). This shift is partly reflected in the increase in the proportion of intermediate-size cysts with time of infection. The pattern for larger cysts shows a general increase in their proportion as a function of the duration of infection which extends from 15 to 27% of the population at weeks 3 and 8, respectively (Table 1). The sole "anomaly" in this pattern is the lower proportion of large cysts at week 4, which is linked to the designation of the cutoffs at 70-$\mu$m diameter, as a cluster of cysts just below this marker (66 to 69 $\mu$m) are found. The lower numbers are also impacted by the fact that fewer tissue cysts were measured at this time point relative to others.

The "reemergence" of large (>70-$\mu$m-diameter) cysts at week 5 and beyond suggests that cyst size does increase during the chronic phase, contributing to the size distribution at the time of inception. In addition, the detection of small tissue cysts (<40-$\mu$m diameter) at later time points may potentially reflect newly formed tissue cysts following reactivation during the chronic phase of infection (Fig. 2B). Together, this evidence points to tissue cysts being dynamic entities, exhibiting a general pattern of expansion during the chronic phase. The reasonable and prevailing assumption has been that larger cysts contain more bradyzoites and that tissue cyst size is governed by the growth of bradyzoites within the cysts (12, 43). In order to directly test these assumptions, we needed to develop a method to directly quantify the number of bradyzoites within tissue cyst sections.

**Development of a method to enumerate bradyzoites within optical sections of tissue cysts.** The heterogeneity of the tissue cysts with regard to their size (Fig. 2C) and physical composition/organization (Fig. 1) suggests that the numbers of resident bradyzoites they accommodate may be variable, even in cysts of the same size. In the course of imaging purified tissue cysts, we routinely use DNA dyes (Hoechst stain or 4′,6′-diamidino-2-phenylindole [DAPI]) that permit the easy identification of tissue cysts based on their characteristic staining patterns in both brain

sections (Fig. 2B) and when purified (see DNA labeling in the figures below). Each bradyzoite contains a single nucleus which provides a direct means of establishing the number of nuclei (and by extension bradyzoites) within any imaged cyst. The largely spherical shape of the nucleus and its size eliminate a shortcoming of directly counting bradyzoites, as the latter are arranged in no particular orientation within the cyst (12, 43). By counting discrete (nonoverlapping) nuclear cross sections, we can accurately establish the number of parasites within the imaged volume defined by an optical z-slice.

We therefore developed a novel image-processing program, BradyCount 1.0 (see Materials and Methods), to directly count the number of discrete nuclei (visualized using Hoechst stain or DAPI) within an optical section of an imaged purified tissue cyst (Fig. 3A). Although the images are two dimensional, they represent a volume defined by the thickness of the optical section, which in turn is dependent on the diameter of the tissue cyst (see the inset of Fig. S2A in the supplemental material). In acquiring the z-stack, we defined the widest z-stack as being the center of the cyst and thereby representing the cyst diameter. A key feature of the program is that it allows the user to implement a thresholding function, using a slider on the screen, to delineate the elements being counted based on their intensity profiles (Fig. 3A; see Materials and Methods). This thresholded image appears adjacent to the DNA image with an outline of each nuclear profile being demarcated as a grayscale image (Fig. 3A). Once the distinct nuclei are outlined, a click on the "count" button (Fig. 3A, red asterisk) enumerates the number of nuclei within the image, which equals the number of bradyzoites present in the optical section. BradyCount 1.0 was tested for accuracy relative to manual counting by three expert individuals (E. Watts, A. Dhara, and A. P. Sinai) and one nonexpert (Y. Zhao) and was found to have an accuracy rate of >95% relative to the mean from manual counting, which was found to be more variable between individuals (data not shown). This novel software for the first time allows the direct and efficient enumeration of bradyzoite numbers within purified *in vivo*-derived tissue cysts. Unlike previous studies where bradyzoite burdens in electron micrographs of tissue cyst sections were manually counted (12, 43), BradyCount 1.0 provides a means to count bradyzoites more efficiently and accurately.

**Tissue cyst diameter/volume does not accurately predict bradyzoite burden within a cyst.** A direct consequence of optimizing the purification of *in vivo*-derived tissue cysts has been the application of imaging approaches to investigate their structural organization. In this study, a total of eight optical sections were acquired for each cyst regardless of the size of the cyst (Materials and Methods; see Fig. S3A in the supplemental material), resulting in
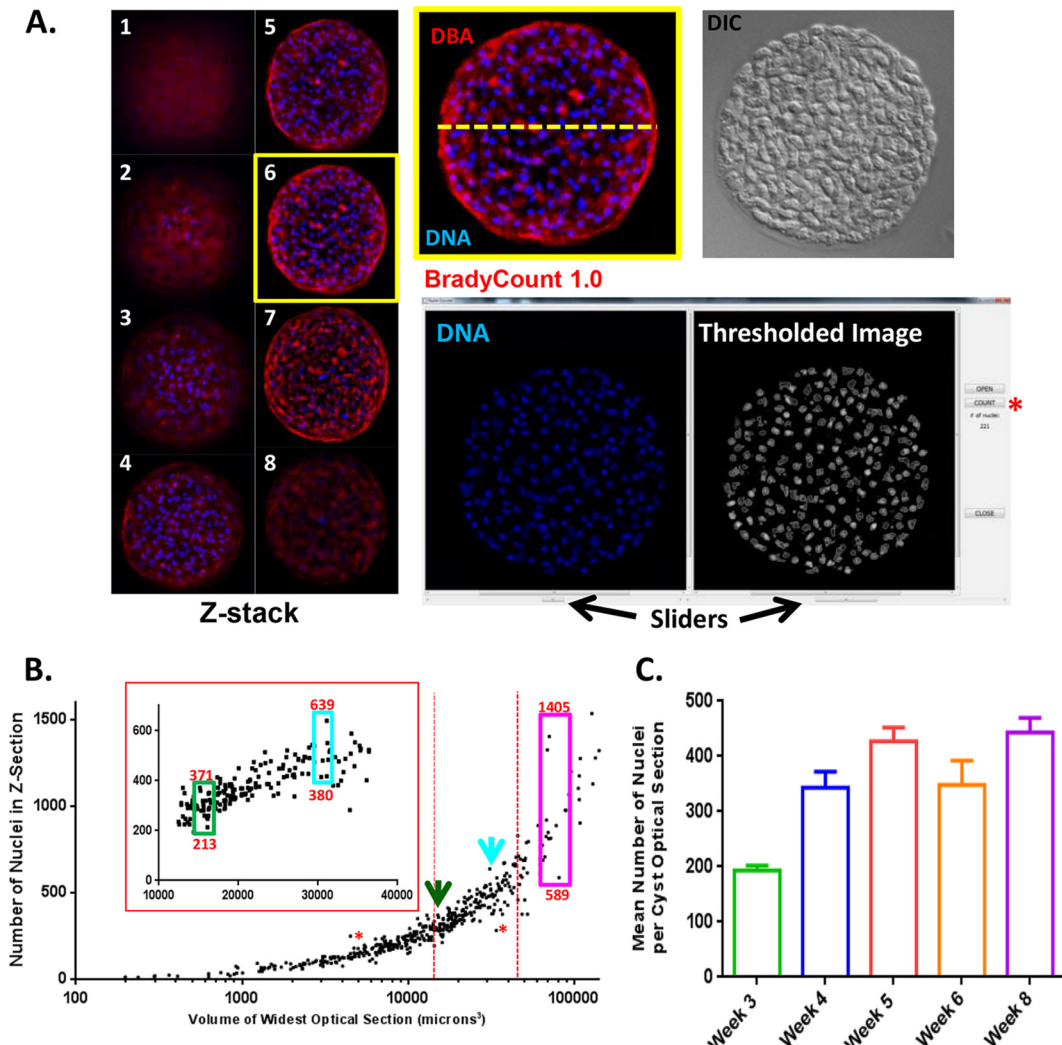
**FIG 3** Establishing the bradyzoite burden within tissue cysts using BradyCount 1.0. (A) A z-stack of a tissue cyst labeled with *Dolichos* lectin (DBA) and Hoechst (DNA) spanning the tissue cyst in eight optical sections. The central section (yellow box) was selected, and the diameter (yellow dashed line) was recorded. A DIC image of the specific cyst is adjacent to the fluorescent image. The DNA image is opened in the BradyCount 1.0 application where a screen grab with two panels reveals the DNA image (left) and the Otsu-transformed (thresholded) image (see Materials and Methods) (right). Sliders under the images allow for the adjustment of the thresholding level such that each discrete nucleus is outlined in the right panel. Clicking the count button (red asterisk) counts the nuclear profiles, which correspond directly to the number of bradyzoites. (B) Nuclear (bradyzoite) counts from 463 tissue cysts harvested at all time points plotted against the imaged volume (i.e., the widest optical slice) revealed a general pattern whereby larger tissue cysts tend to harbor more bradyzoites. However, for all size ranges, considerable heterogeneity in bradyzoite (nuclear) numbers are found (magenta box; green and cyan arrows marking the green and cyan boxes in the inset), indicating that tissue cyst size is not an accurate measure of bradyzoite number. Tissue cysts that have vastly different volumes can contain very similar bradyzoite burdens (red asterisks). (C) The mean bradyzoite burden (plus standard error [SE] [error bar]) for tissue cysts harvested at weeks 3 ($n = 175$), 4 ($n = 30$), 5 ($n = 124$), 6 ($n = 37$), and 8 ($n = 97$) postinfection reveal evidence for bradyzoite replication between weeks 3 to 6, after which the bradyzoite numbers appear to stabilize.

different imaged volumes that were dependent on cyst diameter and the thickness of the slice (diameter divided by 8). This defines the volume of the widest optical section.

We plotted the nuclear (bradyzoite) counts for 463 cysts acquired at all time points to establish the relationship between tissue cyst size and bradyzoite burden. As expected, the first approximation reveals that the number of bradyzoites within tissue cysts increases with tissue cyst volume/diameter (Fig. 3B; see Fig. S2A in the supplemental material). However, this relationship appears to be more complex, as the number of nuclei within tissue cysts of the same size (volume) was found to vary significantly at all size ranges (Fig. 3B [purple box] and inset [cyan and green boxes]). These

differences in bradyzoite burden for similar sized cysts varied significantly, regardless of the size ranges examined as seen with the cyan box (1.79-fold), green box (1.74-fold), and magenta box (2.39-fold) (Fig. 3B). Finally, tissue cysts of vastly differing volumes (diameters) can contain virtually the same number of bradyzoites, as is evident for the cysts marked with the red asterisks (4,502 $\mu$m$^3$, 35.80-$\mu$m diameter, and 250 bradyzoites and 34,004 $\mu$m$^3$, 70.24-$\mu$m diameter, and 282 bradyzoites) (Fig. 3B). Taken together, these data indicate that tissue cyst diameter (volume) is not an accurate predictor of bradyzoite burden.

We sought to establish whether the bradyzoite burden within tissue cysts varied as a function of the time of infection. The mean

bradyzoite burden within the widest optical slice was established for the cysts harvested at weeks 3, 4, 5, 6, and 8. Of note, we did not take into account cyst size (Fig. 2C) when establishing the absolute bradyzoite number, knowing that bradyzoite numbers increase as a general trend with cyst size (Fig. 3B). The data demonstrate that bradyzoite replication must have occurred between weeks 3 (mean, 194) and 4 (mean, 344), with the mean bradyzoite burden increasing 1.8-fold (Fig. 3C). A smaller increase (1.24-fold) is observed between weeks 4 (mean, 344) and 5 (mean, 427) indicative of continued growth, albeit at a reduced rate (Fig. 3C). Finally, the mean bradyzoite burden between weeks 5 (mean, 427) and 8 (mean, 444) stabilizes (Fig. 3C) despite week 8 tissue cysts containing larger (>70-mm) tissue cysts (Table 1). The small dip in the mean bradyzoite burden observed at week 6 is not statistically significant and may have been caused by the smaller number of tissue cysts measured at this time point (Fig. 3C). Together, these data strongly point to active but nonuniform replication occurring within tissue cysts during the chronic phase of infection.

**Packing density as a measure of relative bradyzoite burden.** In attempting to establish potential mechanisms that could explain the basis for the variability in bradyzoite burden within cysts of the same size (Fig. 3B), we sought to establish a metric for the relationship between bradyzoite number and cyst volume. Given that we can capture only a snapshot of a given tissue cyst but not its history or its potential fate, we sought to establish criteria by which insights into bradyzoite dynamics within cysts could be derived. In order to achieve this, we developed the concept of the packing density (PD) which defines the number of bradyzoites ($N$) (based on nuclear profiles determined using BradyCount 1.0) within the volume of the widest optical slice [$\pi r^2 \times$ (cyst diameter/number of z-sections) where $r$ is the radius] on the tissue cyst. This ratio allows for the comparison of bradyzoite burdens within tissue cysts regardless of their size or level of maturity. Of note, the early morphological studies by Ferguson and colleagues (11, 12, 43) reported the presence of both highly packed tissue cysts as well as other cysts that are loosely packed, with the space between bradyzoites filled with a "moderately electron-dense" or "electron-lucent" ground substance. The detection in these early studies of a low level of degenerating ME49 bradyzoites within tissue cysts (12, 43) may contribute to regions of low packing density within cysts.

Little to nothing is known about the replication patterns of bradyzoites *in vivo*, as prior studies have examined only tissue cyst size and not the actual bradyzoite burden (42, 48). What we do know from cell culture-based studies is that conversion from tachyzoites to bradyzoites is associated with both a reduction in the replication rate and increased replicative asynchrony within the transitioning vacuole (15). It is well established that tachyzoite replication is highly synchronized, and the dimensions of the parasitophorous vacuole increase proportionately with each round of replication as evidenced by the tight-fitting vacuolar membrane and the absence of significant space between tachyzoites. This is evident when comparing *Toxoplasma* vacuoles with those of *Leishmania* and *Coxiella* where lysosomal fusion, rather than pathogen growth, results in spacious vacuoles (49–51). Thus, if *Toxoplasma* replication is the primary driver of vacuole volume, the packing density of tachyzoite vacuoles is expected to be relatively uniform, regardless of vacuolar size. This relationship would also translate to tissue cysts if bradyzoite replication were the primary driver of increases in cyst volume (Fig. 4, model A) and has been suggested as the primary mechanism de-

termining tissue cyst size (12). Bradyzoite replication events under this scenario would cause a proportional increase in cyst volume, resulting in no net change in the packing density and a flat relationship between size and PD (Fig. 4, model A). Several pieces of evidence, most notably the heterogeneity in the number of nuclei (Fig. 3B) and the distribution in tissue cyst diameter profiles (Fig. 2C) argue against this scenario, effectively uncoupling bradyzoite replication and tissue cyst size. This presents two alternative scenarios that need not be mutually exclusive, impacting events at distinct stages of the chronic phase.

In the first of these two scenarios, we can envision bradyzoites possessing a replication rate that is greater than the rate of cyst expansion at the time of examination (Fig. 4, model B). In this instance, bradyzoite replication would result in an increasing PD with increasing cyst size (Fig. 4, model B). The relative difference in rates of replication and cyst expansion would govern the specific PD at any given time point and whether or when lysis might occur should bradyzoite replication exceed the capacity of the cyst at that time (Fig. 4, model B).

The third overall scenario (Fig. 4, model C) is more consistent with the reduction in the replicative potential of bradyzoites relative to tachyzoites. In this scenario, we would envision cyst expansion outpacing bradyzoite replication, resulting in reduction of the packing density (Fig. 4, model C); this would manifest as a larger but more "hollow" cyst containing relatively fewer bradyzoites. Such "hollow" tissue cysts were noted in the early ultrastructural studies and were prevalent at later time points in infected-mouse brains (12, 43). The rate at which the packing density would decrease would be based on the relative difference in the rates of cyst expansion and potential bradyzoite replication events within that given cyst (Fig. 4, model C). Thus, in the absence of substantial replication, ongoing tissue cyst expansion would result in the lowering of the packing density (Fig. 4, model C, navy blue curve). Immediately after a replication event however, the packing density would increase, with the increase being dependent on the extent of replication. Higher levels of replication would result in a more substantial upward shift in the PD (Fig. 4, model C, red curve), while a lower level of overall replication would result in a smaller shift (Fig. 4, model C, cyan curve). Once the new PD is established, continued tissue cyst growth in the absence of replication would result in the lowering of the PD in a manner dependent on the rate of tissue cyst expansion (Fig. 4, model C).

**Tissue cyst growth is not driven by bradyzoite replication.** The relationship of packing density relative to tissue cyst volume established by the analysis of 463 randomly acquired tissue cysts at all time points unequivocally demonstrates that in general, tissue cyst expansion outpaces bradyzoite replication (Fig. 5A). Thus, while the total number of bradyzoites is on average higher in larger tissue cysts (Fig. 3B), larger tissue cysts tend to be more loosely packed, containing on average fewer bradyzoites relative to their volume (Fig. 5A). As a corollary, smaller tissue cysts, which are potentially less mature and therefore closer to their tachyzoite origins, tend to be more densely packed (Fig. 5A). This would not be expected if bradyzoite replication were the primary driver of tissue cyst size (Fig. 4, models A and B).

The PD reflects the organization of individual tissue cysts. Not surprisingly based on the differences in bradyzoite burden (Fig. 3B), differences in PD are also seen for tissue cysts of the same volume (Fig. 5A [green, cyan, and magenta arrowheads]; the rela-
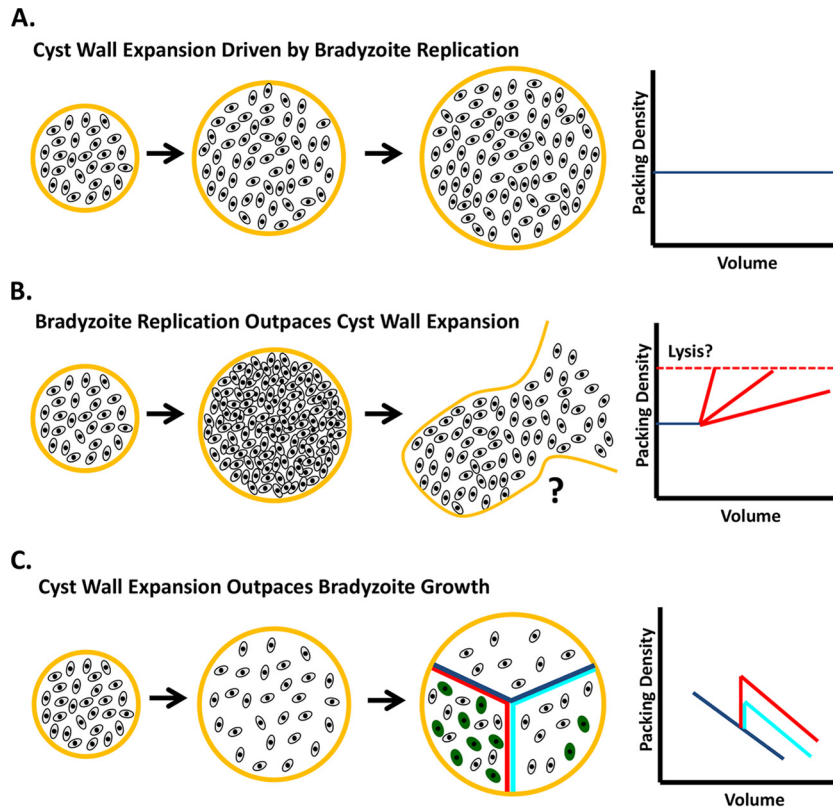
**FIG 4** The packing density as a metric to understand bradyzoite growth with a tissue cyst. The packing density is a ratio of the number of nuclei (bradyzoites) and the volume within which the parasites are housed. This metric can be used to compare the rates of bradyzoite replication and tissue cyst expansion between tissue cysts regardless of their size or time of harvest. (A) This model (model A) posits that the expansion of the tissue cyst is driven by bradyzoite replication. In this scenario, the packing density will not change as a function of cyst volume. In this model, bradyzoite replication and tissue cyst expansion occur proportionately. (B) In this scenario (model B), the expansion of the tissue cyst and bradyzoite replication occur independently of each other, with the replication rate exceeding the rate of cyst expansion. Under this scenario, we would predict an increase in the packing density with increasing cyst volume, which taken to its logical extension will lead to cyst rupture. The likelihood of rupture is determined by the relative rates of bradyzoite replication and cyst expansion. (C) The third scenario (model C) has the rate of cyst expansion outpacing bradyzoite replication, resulting in a volume-dependent reduction in the packing density. Changes in the packing density are possible within a given tissue cyst based on episodes of bradyzoite replication (green bradyzoites). In such instances (red and cyan traces), an increase in bradyzoite number would also proportionately increase the packing density.

tionship of the PD to cyst diameter is presented in Fig. S2C in the supplemental material). In addition, tissue cysts with identical PDs are found to have vastly different volumes (Fig. 5A, the three red asterisks, from left to right, indicate a volume of 847 $\mu$m³ and a PD of 0.024, a volume of 6,450 $\mu$m³ and a PD of 0.021, and a volume of 70,867 $\mu$m³ and a PD of 0.020). Together, these findings suggest that each tissue cyst represents a specific entity that is on its own developmental and replicative course. This course is defined by the dimensions of the tachyzoite vacuole at the time of stage conversion (Fig. 2C and below), the rate of tissue cyst expansion, and the rate and temporal pattern of parasite replication within a given tissue cyst. The packing density effectively integrates the contributions of these elements, providing a means to compare the developmental trajectories of bradyzoites within cysts and the capacity to compare bradyzoite dynamics across tissue cysts.

**Insights into bradyzoite replication patterns within tissue cysts.** A true longitudinal study of bradyzoite development within a tissue cyst is not possible when analyzing purified cysts. This restricts us to representative "snapshots" along the temporal progression from which insights on overall growth patterns must be derived. Once a tissue cyst is established, the packing density is

affected by two disconnected processes during the chronic phase: (i) the expansion of the tissue cyst and (ii) the bradyzoite burden, which is governed by their replication potential and recency of division at the time of harvest. While we do not know the specific rate for each of these processes, the clear lowering of the PD with cyst size suggests that in general, cyst expansion outpaces bradyzoite replication (Fig. 4C and 5A). The question of whether the rates of these events are uniform or change during the course of the chronic infection remains unanswered. In order to address this point, we analyzed the distribution of packing densities for cysts harvested at the different time points, representing discrete snapshots during the course of the chronic infection.

We plotted the mean packing densities for the tissue cyst population in Fig. 3C to determine the relationship between bradyzoite burden and cyst dimensions. The mean packing density at week 3 is likely to directly reflect the contributions of rapid growth as a tachyzoite and the time when stage conversion occurred relative to the time of harvest (Fig. 5B; see Fig. S2D in the supplemental material). The drop in the packing density at week 4 (Fig. 5B), in spite of an increase in the mean bradyzoite burden (Fig. 3C), suggests that expansion of the tissue cyst exceeds the relative replicative capacity at that time point. This pattern is re-
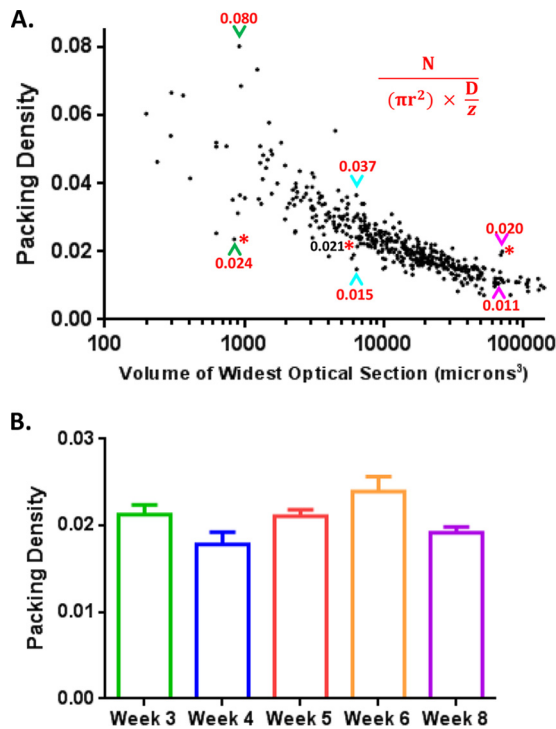
FIG 5 The packing density decreases with increasing cyst volume. (A) The packing density for 463 tissue cysts harvested at all time points plotted relative to the volume of the widest optical section reveals that larger tissue cysts tend to be more loosely packed. These results indicate that the rate of tissue cyst expansion exceeds the replication rate of bradyzoites and occurs independently of bradyzoite replication (scenario C in Fig. 4). The formula used to determine the packing density is shown in red. In this equation, $N$ is the number of nuclei (bradyzoites) in the optical section, $D$ is the diameter of the tissue cyst, $z$ equals the number of optical sections (8 in this case), and $\pi r^2$ is the area of the circle ($r$ is the radius). Of note, smaller tissue cysts tended to be more densely packed while also exhibiting the greatest range of packing densities (green arrowheads). The differences in packing densities for same/similar sized cysts was observed for the intermediate (cyan arrowheads) and large (magenta arrowheads) cysts as well. Finally, tissue cysts of vastly different volumes can have very similar packing densities (red asterisks). (B) The mean packing densities (plus standard errors of the means [SEM] [error bars]) for tissue cysts harvested at weeks 3 ($n = 175$), 4 ($n = 30$), 5 ($n = 124$), 6 ($n = 37$), and 8 ($n = 97$) postinfection reveal evidence of a dynamic and potentially oscillatory pattern where changes in the packing density over the course of the infection reflect the differential rates of cyst expansion and bradyzoite replication. In general, increases in the packing density reflect increased replication rates, while decreases in the packing density are suggestive of tissue cyst expansion in the absence of bradyzoite replication.

versed between weeks 4 and weeks 5 and 6, with an increase in the mean packing density. This shift, viewed in the context of the increased bradyzoite burden (Fig. 3C), would indicate that a slowing of the tissue cyst expansion rate accompanies any further parasite replication. This further reinforces that cyst expansion and bradyzoite replication are not linked and that the dimensions of the cyst are not driven by bradyzoite replication (Fig. 4C). Finally, the maintenance of the relative bradyzoite burden (Fig. 3C) coupled with the increase in the proportion of larger tissue cysts (Fig. 2C and Table 1) at week 8 postinfection likely contribute to the observed reduction in the packing density at this time point. While the current study with the sampling of tissue cysts at intervals between 1 and 2 weeks apart does not provide us with sufficiently fine temporal resolution to define when cyst expansion

and/or replication are occurring, what does emerge are indications for a cyclical pattern. In this pattern, it appears that the expansion of the tissue cyst likely precedes replicative events, although the factors governing them do not appear to be mechanistically linked.

**Capturing bradyzoite replication within _in vivo_-derived tissue cysts.** The diversity of intracyst bradyzoite burden (Fig. 3B), tissue cyst diameter (Fig. 2C), and packing density (Fig. 5) indicate that parasite replication must occur within tissue cysts. The extent to which replication occurs is a matter of controversy in light of the fact that bradyzoites are viewed as dormant largely nonreplicative entities (24). Nonetheless, we sought to capture evidence for bradyzoite replication within purified tissue cysts using the inner membrane complex protein TgIMC3 (_T. gondii_ inner membrane complex protein 3) as a marker to highlight replicating parasites. Indications from the ultrastructural studies suggest the potential for bradyzoite endodyogeny, particularly early in the chronic phase (43, 52).

Asexual stages of _T. gondii_ replicate by an internal budding mechanism referred to as endodyogeny whereby two daughter buds form within the mother and develop into two "newborn" parasites following the turnover of the mother parasite (Fig. 6A) (reviewed in reference 53). The maternal DNA (1.8- to 2n ploidy) segregates between the forming buds, as partially overlapping mitosis and cytokinesis occur in a temporally linked manner (Fig. 6A) (53–55). Work with tachyzoites reveals that the inner membrane complex protein TgIMC3 is present at high levels in the daughter buds during endodyogeny and the newly emergent daughters (56). We reasoned that by tracking TgIMC3 within individual parasites in tissue cysts, we would be able to capture direct evidence for endodyogeny as it occurred.

Despite being considered metabolically and replicatively dormant, parasites within tissue cysts exhibited a considerable frequency of organisms containing each stage of TgIMC3-positive structures associated with the onset (formation of the daughter buds), progression (extension of the daughter inner membrane complex [IMC] and segregation of the nucleus), and completion (release of emergent daughters from the corpus of the mother parasite) of endodyogeny (Fig. 6A). The earliest appearance within gravid mother parasites is the initial formation of the daughter buds as seen in multiple parasites within the tissue cyst (Fig. 6B). One such parasite (with additional examples evident within the same tissue cyst in both the z-section and deconvoluted [Decon] image) is boxed in yellow and highlighted in the DIC and deconvoluted image (Fig. 6B). Within it, two distinct buds and an enlarged nucleus (which appears as a depression in the DIC image) have been captured (Fig. 6B). As endodyogeny proceeds, the inner membrane complex starts to delineate the bodies of the daughter parasites originating from the buds and still within the corpus of the mother parasite (Fig. 6C). In the highlighted example, enlarged within the yellow boxes (Fig. 6C), we have captured not only the profiles of the developing daughters (TgIMC3) but also a bilobe nuclear mass (Fig. 6C) captured as it segregates into the individual daughters (Fig. 6C). The later stages of endodyogeny have also been captured with examples of recent parasite replication within brightly TgIMC3-labeled parasites (Fig. 6D, red and yellow boxes). Here, recently completed nuclear division (Fig. 6D, boxed, yellow asterisks) awaits the completion of cytokinesis as the daughter parasites appear to still be within the gravid mother (Fig. 6D, boxed). Finally, the completion of
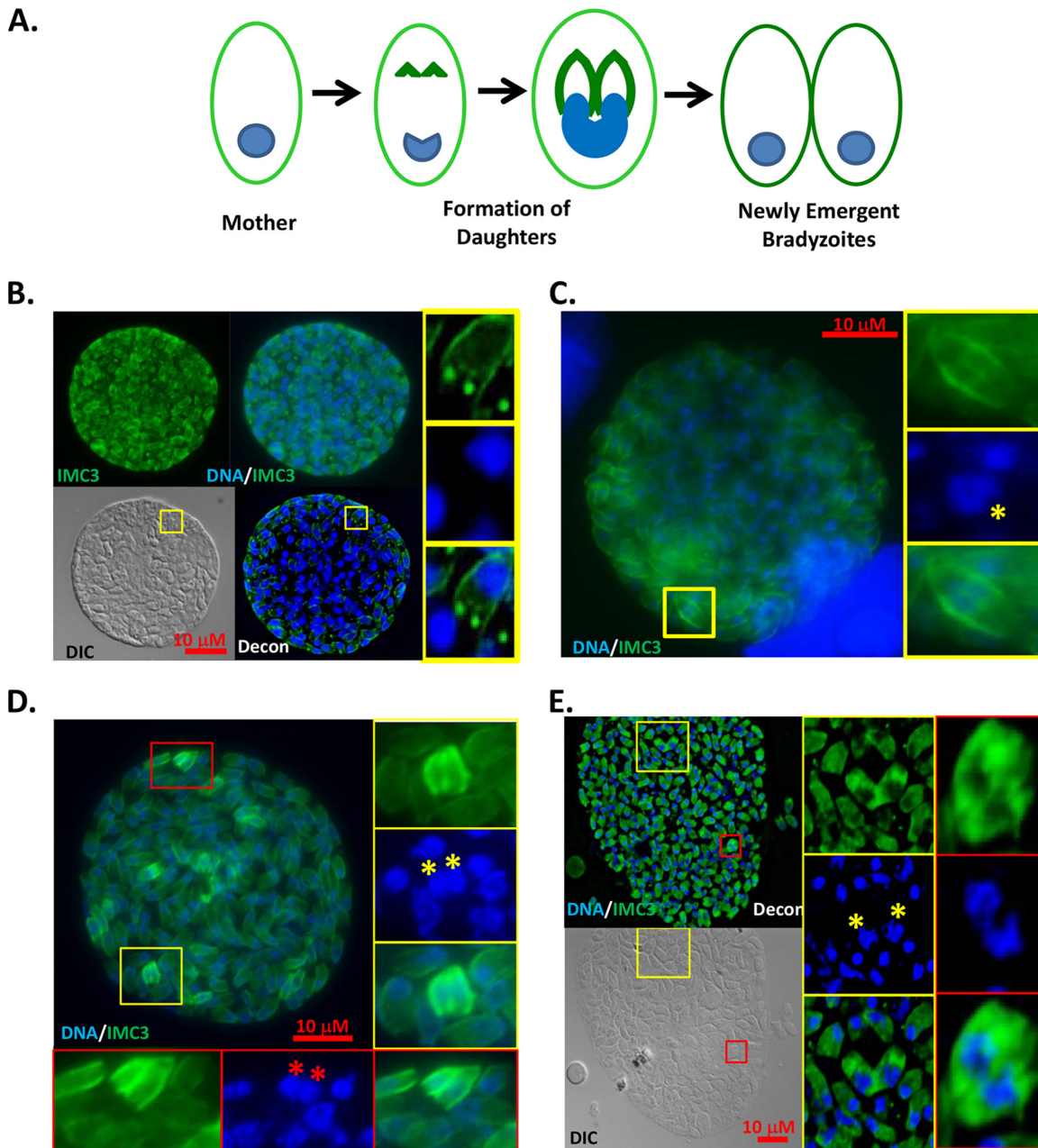
**FIG 6** Evidence for active endodyogeny within purified tissue cysts. (A) Schematic depiction of endodyogeny, revealing the formation of daughter buds visualized by intense TgIMC3 labeling. The newly formed daughter buds extend within the mother, exhibiting high TgIMC3 intensity as nuclear division results in a bilobe nucleus. Finally, upon the completion of endodyogeny, two new parasites emerge following the degradation and recycling of maternal components. (B) Detection of daughter buds in multiple parasites within a cyst detected with anti-TgIMC3 antibody. One of many such examples is highlighted in the yellow box within the DIC and deconvoluted (Decon) image and magnified to reveal both the TgIMC3 and DNA signals (yellow box). Note that the parasite has a single enlarged nucleus that has not initiated mitosis. (C) Elongation of the daughter buds reveals the outlines of the two progeny parasites (yellow box), with the nucleus revealing a distinct bilobe shape as it migrates into the forming daughter cells. (D) Multiple instances of later stages on endodyogeny (red and yellow boxes) reveal intense TgIMC3 labeling of parasites still connected to the maternal residual body. Note that mitosis in these parasites has been completed as each daughter has a distinct nucleus (red and yellow asterisks). (E) A high proportion of emerging TgIMC3-positive daughter parasites within a tissue cyst. Two highlighted examples (yellow and red boxes) reveal a characteristic "V" pattern in separating daughters still attached to the residual body seen in both the TgIMC3 and DIC images (yellow box; yellow asterisks mark their nuclei). Also seen are two recently divided parasites adjacent to each other exhibiting intense TgIMC3 labeling (red box). All the tissue cysts depicted here were harvested at week 3 postinfection. Additional examples are shown in Fig. S3 in the supplemental material.

endodyogeny is evident in a tissue cyst with relatively uniform levels of TgIMC3 labeling across all parasites (Fig. 6E). The emerging daughters are in the final stages of separation (Fig. 6E, yellow and red boxes) evident as the V-shaped orientation in the TgIMC3 labeling and the DIC image (Fig. 6E, yellow box). The nuclei of the recently emergent parasites are indicated by yellow asterisks (Fig. 6E, yellow box). Finally, the completion of endodyogeny noted by the presence of two distinct and adjacent parasites exhib-

iting high levels of TgIMC3 are highlighted in the red boxed area (Fig. 6E). Of note, multiple examples of these later stages of endodyogeny are evident within this cyst (Fig. 6E) with additional examples of all stages of the process observed in subsequent figures and the supplemental material (see Fig. S3 in the supplemental material) that highlight different events in bradyzoite development within *in vivo*-derived cysts.

**Parasites within cysts exhibit diverse patterns of replication.** Tachyzoite replication occurs synchronously, resulting in both even numbers of parasites (55, 57) and uniform levels of TgIMC3 labeling within a vacuole (56, 58). Conversion to bradyzoites is associated with increased replicative asynchrony (15, 38), resulting in odd numbers of organisms, which based on their asynchrony would be predicted to exhibit variable TgIMC3 labeling within a cyst, reflecting when the given parasite last divided. Consistent with increased replicative asynchrony found in tissue culture-derived cysts (15, 38, 39), we detected evidence for isolated replication (Fig. 7A, top panel) where one or a few scattered parasites were found to be undergoing endodyogeny at all time points postinfection (data not shown). More frequently, however, asynchronous replication was observed in clusters within cysts regardless of whether cysts were "early" (e.g., week 3 [Fig. 7A, middle panel] or 4 [not shown]) or later (weeks 5 to 6 [not shown] and week 8 [Fig. 7A, bottom panel]). Notably, when clusters of replicating parasites were observed, the localized density of nuclei was found to be consistently greater (Fig. 7A, middle and bottom panels, yellow dashed regions) than areas which were not actively dividing (Fig. 7A, middle and bottom panels, red dashed regions). The detection of clustered growth within cysts suggests that tissue cysts are not uniform entities but rather heterogenous communities of genetically identical but phenotypically distinct members. Somewhat surprisingly, we also detected apparently synchronous replication where all the bradyzoites appeared to be cycling in unison. This included instances of moderate synchrony (with more than 75% of imaged parasites exhibiting uniform levels of TgIMC3 labeling) (Fig. 7B, top panel) or high levels of synchrony at both early (week 3 [Fig. 7B, middle panel]) and late (week 8 [Fig. 7B, bottom panel]) time points as well as cysts at weeks 4 to 6 (data not shown). Evidence for synchronous replication could explain the roughly twofold increase in both the number of nuclei (Fig. 3B) and the packing density of tissue cysts of identical volume (Fig. 5A). Finally, in rare instances, particularly in larger (>70-$\mu$m-diameter) cysts, peripheral replication patterns and "waves" of replication were apparent (see Fig. S5 in the supplemental material), which suggests that replication patterns may be influenced by nutrient distribution and/or signaling systems yet to be identified. Of note, the limitations associated with examining single thin sections by electron microscopy (1-$\mu$m sections were used) (12, 43) severely compromised the ability to detect these patterns within tissue cysts. This would contribute to a gross underrepresentation of the extent of replication within tissue cysts. In contrast, the thickness of an optical section in a 60-$\mu$m tissue cyst being visualized is 7.5 $\mu$m, effectively imaging whole parasites, ensuring detection of replicative events in progress.
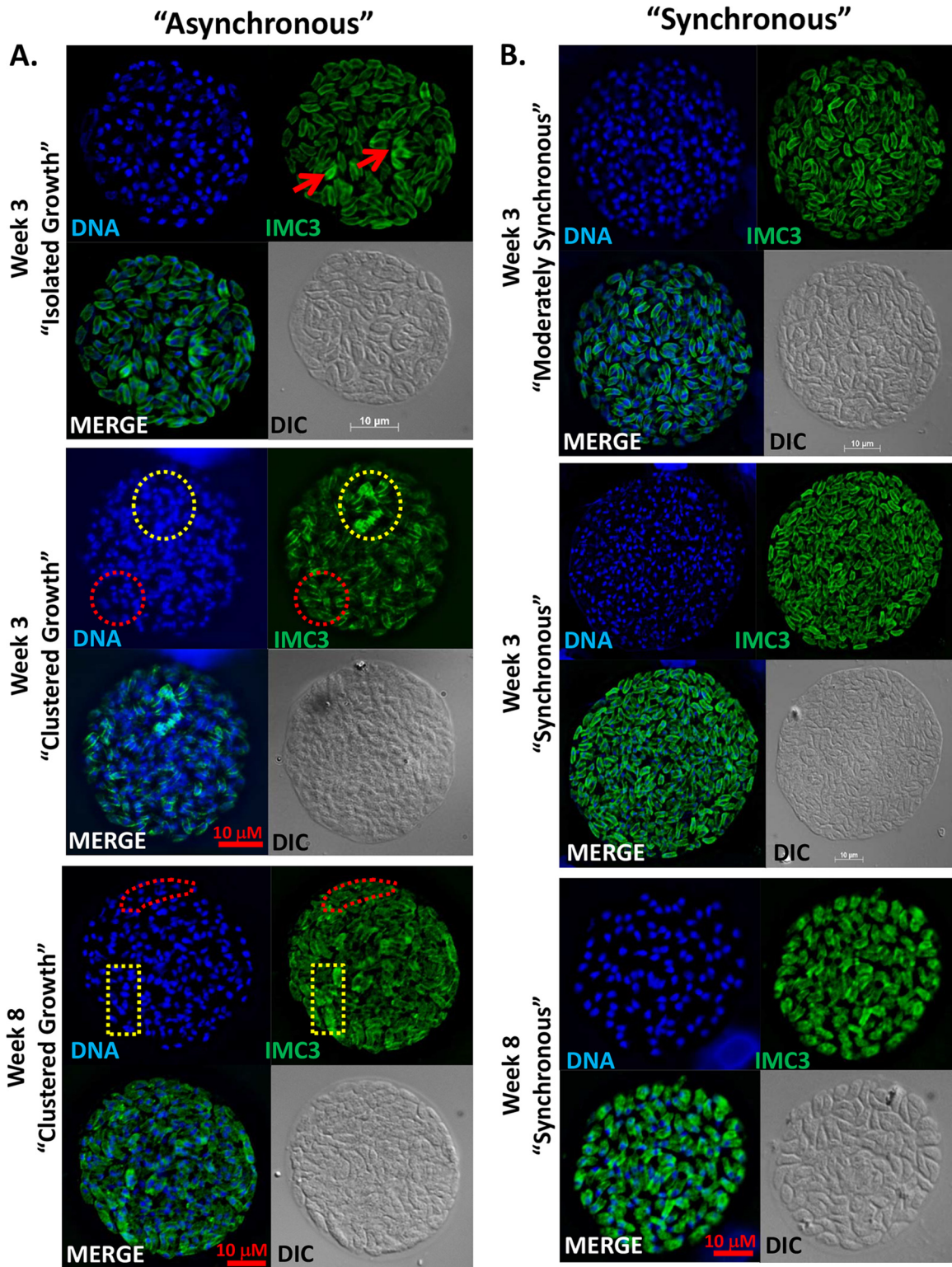
**The replicating parasites within tissue cysts are bradyzoites.** Among the arguments that have been used to explain parasite replication within tissue cysts is that individual parasites (or clusters of parasites) exhibiting replication represent organisms that have dedifferentiated to tachyzoites, thereby acquiring replicative properties (24). The reported presence of "mixed" cysts contain-

ing both tachyzoites and bradyzoites specifically for ME49 parasites (43) may suggest that this is the basis for replication within tissue cysts. Several markers can be used to distinguish bradyzoites from tachyzoites. Among them, the surface antigens TgSAG1 (tachyzoite specific) and TgSRS9 (bradyzoite specific) have been validated at both the transcriptomic and protein levels in both cultured cells and *in vivo* cysts (28, 30, 35). Given that a small number of replicating parasites within a tissue cyst may be missed using nonmorphological criteria, we examined whether individual parasites undergoing endodyogeny (based on TgIMC3 labeling) were TgSRS9 (bradyzoite) or TgSAG1 (tachyzoite) positive. In general, labeling tissue cysts with anti-TgSRS9 antibody results in extensive staining, revealing the outlines of individual bradyzoites and also staining the amorphous matrix between parasites (Fig. 8A). Labeling with anti-TgSRS9 antibodies clearly demonstrates that the parasites within cysts exhibiting both asynchronous and synchronous replication are in fact bradyzoites (Fig. 8A; additional images in Fig. S5 in the supplemental material).

In order to confirm the absence of the tachyzoite marker TgSAG1, we labeled tissue cysts with anti-TgIMC3 and anti-TgSAG1. In the vast majority of tissue cysts, no labeling of parasites was evident using anti-TgSAG1 antibody in either largely asynchronous cysts (Fig. 8B, top panel) or more-synchronized cysts (Fig. 8B, bottom panel). The specific example (Fig. 8B, top panel) was selected, as it exhibits the highest level of TgSAG1 labeling observed, which is just above background levels. Additional images of TgIMC3- and TgSAG1-labeled tissue cysts are presented in Fig. S6 in the supplemental material where we focus on images that have the highest levels of TgSAG1 staining detected. In addition, we were able to capture very immature tissue cysts containing clearly replicating parasites within immature cysts (based on the thin cyst walls using *Dolichos* [DBA] lectin labeling) which were TgSAG1 positive (Fig. S6C and S6D). These tissue cysts, which were captured in the act of differentiating, were found to be extremely fragile, with most not surviving the purification process (data not shown).

**TgIMC3 serves as a marker to "birth date" bradyzoites within tissue cysts.** TgIMC3 was identified as a marker of developing and recently emergent parasites during endodyogeny in tachyzoites, as their labeling intensity is considerably brighter than that of the mother parasite (56, 58) (Fig. 9A). Furthermore, the decay of TgIMC3 intensity was found to occur over time (56), with signal being restored upon a subsequent round of replication (Fig. 9A). The specific rate for the loss of TgIMC3 intensity has not been determined for either tachyzoites or bradyzoites, although the heterogeneity evident in tachyzoite populations suggests that it likely dissipates within the typical doubling time of 8 to 12 h for type II ME49 tachyzoites (data not shown). This rate of TgIMC3 decay in bradyzoites may be considerably slower if in fact the decay rate is a function of the duration of the cell cycle or time between replicative events. Notwithstanding this gap in our knowledge, TgIMC3 intensity can serve as a relative measure of the "age," defined as the time since the "birth" of a given bradyzoite within the tissue cyst (see asynchronous replication in Fig. 7 and 8). The heterogeneity in TgIMC3 intensity is not restricted to only individual bradyzoites within cysts but is also observed across cysts purified from the same mouse brains where randomly acquired cysts recorded at the same exposure on the same slide exhibit considerable variability with regard to both labeling intensity and pattern (see Fig. S7 in the supplemental material).

**FIG 7** Patterns of replication within tissue cysts. (A) The predominant pattern for parasite replication within *in vivo* tissue cysts was found to be asynchronous. This included isolated growth where individual parasites were actively replicating (top panel) or the more frequent clustered growth (middle and bottom panels) where multiple parasites adjacent to each other were replicating as a group (yellow dotted outline), while other areas within the tissue cyst contained parasites that were not replicating at the time of harvest (red dotted outline). The density of parasite nuclei in areas with active replication was typically higher than those in areas where active replication was not observed (middle and bottom panels; DNA panels). Asynchronous replication was observed well into the chronic phase seen in a week 8 tissue cyst (bottom panel). (B) Moderately (top panel) and highly synchronized (middle and bottom panels) replication where a significant majority or all parasites appeared to be replicating at the same time were detected both early (week 3 [top and middle panels]) and later (bottom panel) time points. Additional examples as well as rare ordered patterns of replication are presented in Fig. S4 in the supplemental material.
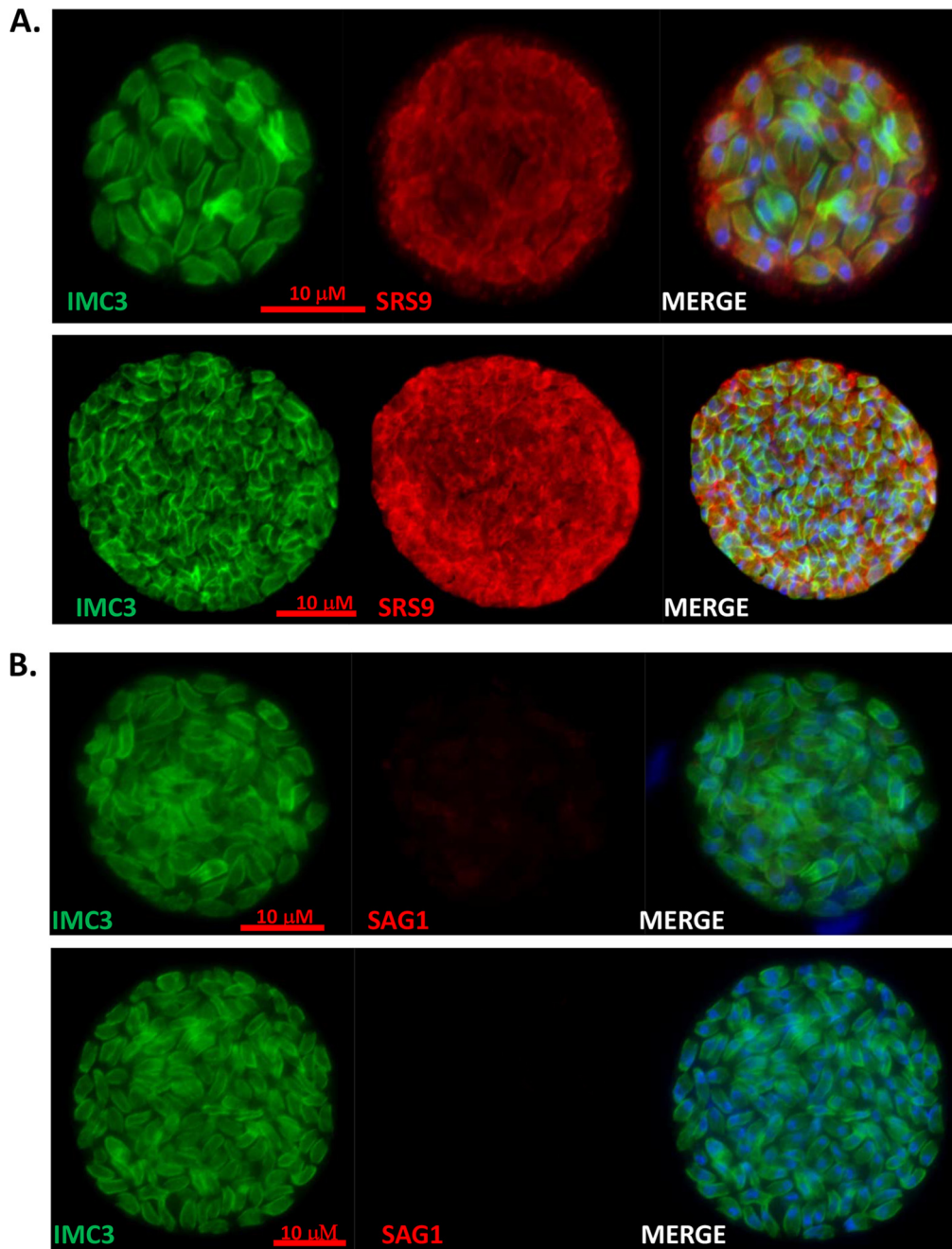
FIG 8 Replicating parasites within tissue cysts are bradyzoites. (A) Tissue cysts containing actively replicating parasites based on the TgIMC3 labeling pattern contain organisms that label with the bradyzoite-specific surface marker TgSRS9, indicating that they are bradyzoites. (B) Parasites within tissue cysts containing actively replicating (based on TgIMC3 labeling) parasites fail to label with the tachyzoite-specific marker TgSAG1. An example of both the highest level of TgSAG1 labeling (top panel) and typical labeling (bottom panel) are shown. The top rows in panels A and B each depict week 3 cysts, while the bottom rows depict week 8 cysts. Additional images of TgSRS9 and TgSAG1 labeling in tissue cysts, including images of immature cysts (based on thin DBA-positive cyst walls) where elevated TgSAG1 intensity is observed are presented in Fig. S5 and S6 in the supplemental material.

Given that the relative TgIMC3 intensity varies as a function of the time defined by the time since the last prior round of replication, we reasoned that it could serve to effectively "birth date" individual bradyzoites. This principle can be applied to the whole cyst whereby TgIMC3 intensity would report on the mean "age" of all the bradyzoites within that cyst. Statistically, tissue cysts bearing actively replicating bradyzoites would present higher levels of

TgIMC3 relative to cysts within which bradyzoites had not replicated for a longer time period. In addition, cysts where extensive/synchronous replication had recently occurred would be more intensely labeled than cysts within which bradyzoites replicated at the same time but did so asynchronously or sporadically.

In order to establish whether tissue cysts harvested at distinct time points postinfection varied with regard to their replicative
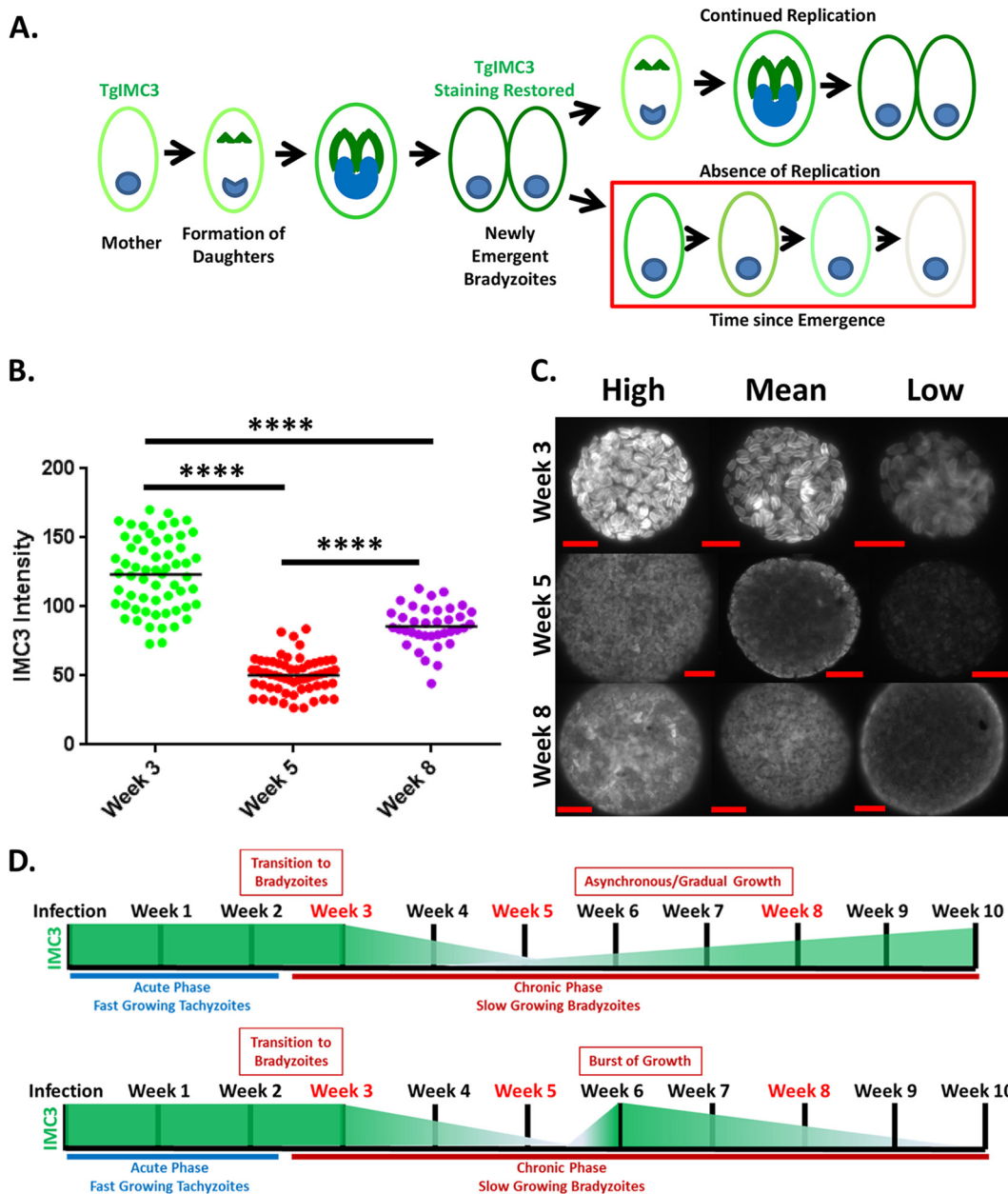
**FIG 9** TgIMC3 as a marker to "birth date" bradyzoite replication within tissue cysts. (A) Following an initial round of replication, emergent bradyzoites possess a strong TgIMC3 signal. In the absence of further replication, this signal dissipates with currently unknown kinetics (red boxed profile). In contrast, continued replication resets TgIMC3 intensity levels. (B) Tissue cysts harvested at weeks 3, 5, and 8 were stained at the same time with the same aliquots of TgIMC3 antibody. All images were acquired at random and at a fixed exposure. The mean TgIMC3 pixel fluorescence intensity was normalized to the imaged area of the cyst established. The intensity of TgIMC3 protein expression from 157 cysts (week 3 [$n = 60$], week 5 [$n = 60$], week 8 [$n = 37$]) was analyzed for cysts from three different weeks postinfection. One-way ANOVA demonstrates significant differences for TgIMC3 expression between weeks 3, 5, and 8 ($F_{2,154} = 214.9$; $P < 0.0001$ [indicated by four asterisks]). Tukey's pairwise multiple-comparison test ($\alpha = 0.05$) indicated that the mean intensity of TgIMC3 labeling of cysts harvested at each time point differed significantly from one another. The data indicate that tissue cysts harvested at week 3 are brightest, consistent with relatively recent or concurrent replication based on the level of TgIMC3 labeling. Tissue cysts at week 5 exhibit low overall levels of TgIMC3 intensity, while those harvested at week 8 have an intermediate level consistent with significant replication having occurred between weeks 5 and 8. (C) Representative images of tissue cysts defining the high, mean, and low TgIMC3 intensity levels for each population of cysts reveal not only different overall levels of TgIMC3 but also distinct patterns of labeling. (D) Potential models explaining the patterns of TgIMC3 between weeks 3 and 8. Rapid replication during the tachyzoite phase accounts for elevated TgIMC3 labeling that accounts for week 3 labeling exhibiting the brightest cysts with the greatest diversity. A reduction in growth rate, manifesting as greater intervals between replicative events, accounts for the decreased mean TgIMC3 intensity at week 5. The intermediate levels for TgIMC3 at week 8 can be accounted for by two distinct, although nonexclusive, models. In the first model, gradual, likely asynchronous growth results in a net increase in TgIMC3 intensity. Alternatively, a burst of replication within the population (depicted here between weeks 5 and 6), followed by an absence of replication and a time-dependent loss of TgIMC3 intensity, results in intermediate levels within cysts captured at week 8 postinfection.

capacity, we harvested cysts at weeks 3, 5, and 8 postinfection and labeled them at the same time with the same aliquot of antibody, recording images under identical exposure level conditions (see Materials and Methods). The relative mean TgIMC3 labeling intensity (normalized to the size of the cyst in the optical section) was established using NIH ImageJ. As expected, tissue cysts purified at week 3 exhibited overall high levels of TgIMC3 labeling, indicating that the bradyzoites had recently last divided, potentially as tachyzoites prior to stage conversion (Fig. 9B). Examples of cysts with the highest staining intensity, mean staining intensity, and lowest staining intensity for each time point are presented in Fig. 9C. The same exposure settings were used to acquire images of week 5 and week 8 tissue cysts and establish the relative mean TgIMC3 intensities for cysts at these time points (Fig. 9B and C). What is readily apparent is that TgIMC3 intensity is markedly lower in week 5 cysts than in week 3 cysts, indicating that the time interval from the preceding replication event to the time of harvest exceeded the time frame for TgIMC3 decay. However, this does not mean that no replication occurred between weeks 3 and 5, a position supported by the increase in mean bradyzoite burdens in this time frame (Fig. 3C). Although the mean bradyzoite burden was largely unchanged between week 5 and week 8 tissue cysts (Fig. 3C), the detection of TgIMC3 labeling levels intermediate to those between weeks 3 and 5 (Fig. 9C) is consistent with continued bradyzoite replication occurring within tissue cysts *in vivo* between weeks 5 and 8 postinfection. The intermediate level of TgIMC3 intensity (Fig. 9C) suggests that when bradyzoite replication does occur, it appears to happen asynchronously, resulting in a proportionate increase in the mean TgIMC3 intensity (Fig. 9D). We cannot, however, rule out the possibility that a significant burst of replication occurs and that the intermediate TgIMC3 intensity at the time of harvest reflects the waning signal after replication (Fig. 9D). The different likelihood of bradyzoite replication as a function of the time of harvest was supported by direct examination of the tissue cysts represented in Fig. 9B. Here we detected at least one actively replicating or recently divided (TgIMC3-bright) bradyzoite in 98% of week 3 tissue cysts, 69% of week 5 tissue cysts, and 97% of week 8 tissue cysts.

We wanted to establish whether there was any relationship between replicative capacity and tissue cyst size. The absence at week 3 of any correlation between TgIMC3 intensity and tissue cyst size (Fig. 10A, green dashed line; mean diameter, 41 $\mu$m) supports the idea that the size of these cysts was likely determined by their size at the time of tachyzoite-to-bradyzoite conversion and not significantly contributed to during the short chronic phase at this early time point. In this population, the dimmer cysts (based on TgIMC3 intensity) are presumed to have formed earlier in the infection process than the brighter ones (Fig. 9A and 10A). The finding at week 5 of considerably larger tissue cysts (Fig. 10A, red dashed line; mean diameter, 58 $\mu$m) (Table 1), all of which had low TgIMC3 staining relative to the week 3 population (Fig. 9B and 10A) suggests that bradyzoite replication that may have occurred earlier (Fig. 3C) in this time interval accounted for the low TgIMC3 intensity, while tissue cyst expansion continued independently (Fig. 10A). This expansion of the tissue cysts is maintained at week 8 (Fig. 10A, purple line; mean diameter, 67 $\mu$m) (Table 1) and was accompanied by some relatively recent (between weeks 5 and 8) replication that occurred preferentially within the smaller week 8 cysts (Fig. 10A). The individual relation-
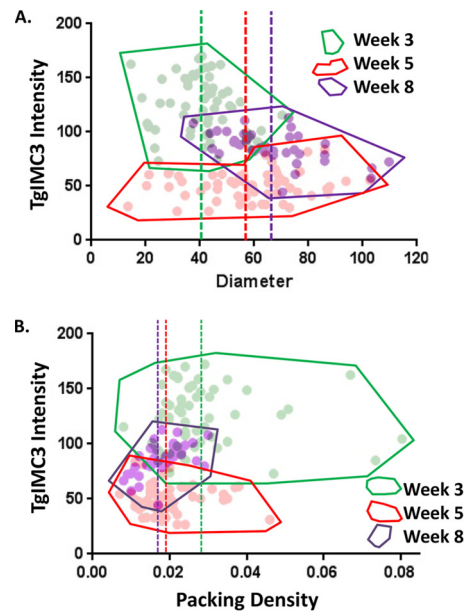


**FIG 10** Relationships between recency of replication, tissue cyst size, and packing density. (A) The relationship between TgIMC3 intensity and tissue cyst size for the cysts harvested at weeks 3, 5, and 8 was plotted. The growth of tissue cysts noted by the shift in the mean tissue cyst diameter (vertical dashed lines; 41 $\mu$m at week 3, 58 $\mu$m at week 5, and 67 $\mu$m at week 8) does not correlate with the recency of parasite replication based on TgIMC3 intensity, emphasizing that parasite replication does not dictate tissue cyst size. Cysts harvested at week 3 exhibit no pattern between TgIMC3 intensity and cyst diameter. This pattern is preserved for week 5 cysts where cyst expansion has occurred, but no significant recent replication is detected. In contrast, tissue cysts harvested at week 8 exhibit an inverse relationship whereby smaller cysts are more likely to contain recently replicated parasites (higher TgIMC3) relative to the larger tissue cysts. (B) The relationship between TgIMC3 intensity (recency of replication) and packing density integrates the bradyzoite burden and tissue cyst size, thereby linking the consequences of both replication and size. Tissue cysts harvested at week 3 or 5 do not exhibit any distinct pattern between TgIMC3 intensity and the packing density with the exception of a significant shift down in the packing density at week 5. This is entirely consistent with the increase in tissue cyst size in the absence of significant replication (low TgIMC3). Notably, replication occurring between weeks 5 and 8 (purple) results in a positive relationship, indicating that the upward shift in the packing density must be related to new replication noted by the intermediate TgIMC3 intensity levels. The mean packing density for the different weeks were as follows: 0.0278 for week 3, 0.0196 for week 5, and 0.0180 for week 8. The imaged cysts used in these analyses are the same as those acquired in Fig. 9B.

ships between cyst diameter and TgIMC3 intensity at the three time points are presented in Fig. S8A in the supplemental material.

Integration of TgIMC3 intensity with tissue cyst size (Fig. 10A) as a function of the duration of infection introduces a temporal component to examining both tissue cyst dynamics and the timing of parasite replication within tissue cysts. Using BradyCount 1.0, we established the bradyzoite burden for this population of tissue cysts and used this information to determine whether the duration of infection-dependent patterns in the packing density could be established. We therefore plotted the specific packing densities for the cysts harvested at weeks 3, 5, and 8 in Fig. 9 relative to the TgIMC3 intensity levels (Fig. 10B). Tissue cysts harvested at week 3 exhibited the broadest range of packing densities and had the highest mean packing density (Fig. 10B, green dashed line; mean, 0.0278). In light of their relative temporal closeness to the tachyzoite state, the overall higher packing density

and detection of the most highly packed cysts are not surprising. The pattern for week 5 cysts is distinctive in that the consistently low TgIMC3 levels (Fig. 9B and 10B) correlate with a markedly reduced mean packing density (Fig. 10B, red dashed line; mean, 0.0196). This finding reinforces that tissue cyst expansion outpaced parasite replication and the replication that did occur happened earlier in the time interval, as marked by the overall low intensity for TgIMC3 (Fig. 10B). It is also notable that the tissue cysts with the higher packing densities (>0.0230) tend to have higher TgIMC3 levels, indicating more recent replication relative to the other tissue cysts in this pool (Fig. 10B). The exception is the lone cyst with the highest packing density (0.046) in which neither cyst expansion nor recent parasite replication appears to have occurred (Fig. 10B).

The increase in overall TgIMC3 intensity observed at week 8 is consistent with the cumulative effects of either asynchronous replication or an episode of replication between weeks 5 and 8 captured as the signal waned (Fig. 9D). Notably, while the patterns for the packing density distributions are similar for weeks 3 and 5 (shape and orientation of the trapezoids) (Fig. 10B), the cysts harvested at week 8 exhibit a markedly upward trajectory, indicating that tissue cysts containing higher TgIMC3 intensities are more densely packed (Fig. 10B). The individual relationships between packing density and TgIMC3 intensity at the three time points are presented in Fig. S8B in the supplemental material. This apparent shift in the packing density is consistent not only with parasite replication within tissue cysts, but it also supports a potential temporal relationship whereby tissue cyst expansion may precede parasite replication events. Whether this occurs stochastically, given the apparent absence of functional linkage between these events, or is regulated is not currently known.

## DISCUSSION

In spite of their central role in the pathogenesis of toxoplasmic encephalitis in the immune suppressed, little is known about the biology of bradyzoites and the tissue cysts within which they are housed. This paucity of knowledge is particularly acute in the realm of *in vivo* infections where technical challenges have served as a significant barrier to detailed cell biological and biochemical analyses. As a result, even the most basic questions regarding the replicative capacity and pattern of bradyzoites within tissue cysts *in vivo* remain largely unknown. Studies of this life cycle stage have focused on the tissue cyst itself rather than the bradyzoites that they house. As a result, the determinants being measured when examining the effects of drugs (52, 59–63) or changes in immune status (6, 64–67) during the chronic phase have measured tissue cyst number and dimension while limiting analyses on bradyzoites themselves to nonquantitative morphological descriptions.

In an attempt to address these basic questions in bradyzoite replication, we sought to optimize the purification of tissue cysts from infected-mouse brains as the first but crucial step to more-detailed analysis. A modification of the classic Cornelissen protocol (41) coupled with the standardization of methods for harvesting gradients and enumerating tissue cysts (Fig. 1A; see Text S1 in the supplemental material) provided considerable insights into the physical composition of tissue cysts, indicating a previously unrecognized level of heterogeneity in tissue cyst density (Fig. 1B and C). An important caveat in our studies is that we examined a single parasite strain (*T. gondii* ME49) in a single mouse background (CBA/J), fully appreciating that differences in the progres-

sion of the chronic phase will be found in other strains and combinations of both parasite and host. In addition, we focus exclusively on CNS-derived tissue cysts, acknowledging that the progression of bradyzoite and cyst development may differ in other tissues.

The compilation of data accumulated over a 2-year period involving a total of 99 independent tissue cyst purification gradients harvested between 3 and 8 weeks postinfection revealed changes in tissue cyst composition and organization as a function of the time of infection (Fig. 1B and C), together suggesting that a dynamic maturation of cysts must occur *in vivo* despite tissue cysts and bradyzoites being considered dormant entities.

Consistent with earlier findings (43), the yield of purified tissue cysts was found to be remarkably uniform across the time scale examined (Fig. 2A and Table 1). One interpretation of this finding is that tissue cysts and by extension the bradyzoites that they house are dormant, metabolically inert, and immunologically invisible entities. Data presented in this study indicate that bradyzoites and tissue cysts are not quiescent, while several more-recent studies indicate that tissue cysts may not be as "invisible" to the immune system as previously imagined (64, 65, 68–71). The only way in which one can resolve the uniformity of tissue cyst yields between weeks 3 and 8 postinfection is to consider that the loss of a tissue cyst is balanced by the emergence of, on average, just one cyst. When one considers that a tissue cyst may contain several thousand bradyzoites (Fig. 3B), the absence of an increasing cyst burden over time, in the face of documented reactivation (Fig. 2B) speaks to the efficiency of immune clearance in preventing large-scale reseeding of new infection sites in the brain.

A well-established feature of tissue cysts at any given time point is the heterogeneity in their size (diameter/volume). The direct measurement of 630 tissue cysts exhibits a broad size range across all time points (Fig. 2C). A more careful examination (Table 1) reveals that the average tissue cyst grows in diameter (volume) over time (mean diameters in Table 1). In addition, the proportion of large size (>70-μm-diameter cysts) increases with the duration of the chronic phase (Fig. 2C and Table 1). However, despite the generally upward progression in size, we can readily detect smaller tissue cysts at the later time points, suggesting that these may be newly seeded cysts (Fig. 2B and C). The proportion of these smaller cysts remains stable between weeks 5 and 8, well into the chronic phase, suggesting that continuous low-level reactivation must occur in the CBA/J background as has been previously reported (64, 72–74). Examination of other permissive (C57B/6) or less-permissive (BALB/c) backgrounds may provide insights into the reactivation/reseeding processes and the impact of the host immune context on these processes (64, 72–74).

We were somewhat surprised by the frequency of large tissue cysts (>70 μm in diameter) in light of the fact that neurons and astrocytes, two cell types associated with housing cysts *in vivo*, do not have the physical capacity to house such large cysts within their cell bodies. A clue as to the site of development emerges from recent imaging studies from the Koshy laboratory (75) which appear to show cysts associated with peripheral neuronal processes such as dendrites and not the cell body (or soma) of the neurons when imaging thick brain sections by confocal microscopy (Anita Koshy, University of Arizona, personal communication). The plasticity of dendrites/axons coupled with the availability of surplus membranes following their retraction may allow for intracellular development of large cysts away from the cell body. It is

tempting to speculate that an increasing body of literature connecting chronic toxoplasmosis to behavioral changes in rodents (76) and neurological syndromes in humans (77, 78) may be contributed to by the loss of normal neuronal connections due to the retraction of dendrites driven by tissue cyst expansion.

The heterogeneity in tissue cyst size (Fig. 2C and Table 1) does not yield information on the relationship between cyst volume and the actual bradyzoite burden. Our development of the Brady-Count 1.0 imaging software permits for the first time the efficient quantitation of bradyzoite numbers in captured optical sections (Fig. 3A). While the data (Fig. 3B) generally support the contention that larger tissue cysts contain more bradyzoites, the observation that identically sized tissue cysts can differ in their bradyzoite burdens by more than twofold reveals the importance of looking directly at the number of bradyzoites. This analysis further reveals that tissue cysts cannot be considered monolithic entities and the significant variation between cysts is potentially due to the bradyzoites being dynamic entities; we have now begun to learn about the patterns of development.

The capability to directly establish true relative bradyzoite burdens within cysts and by extension populations of cysts exposes for the first time insights directly into the dynamics of bradyzoite growth *in vivo*. We therefore examined whether the progression of the chronic phase is associated with an increase in actual bradyzoite numbers (given that the mean tissue cyst yields are fairly constant [Fig. 2A]). Our findings demonstrate not only that the number of bradyzoites increase but also that bradyzoites exhibit differential growth profiles as the chronic phase progresses (Fig. 3C; see Fig. S2 in the supplemental material). The utility of such analyses in establishing the effects of drug treatments *in vivo* is that they will permit direct quantification on how treatments may affect bradyzoites, which could be masked when looking only at tissue cyst numbers, as is currently done (52, 59–63).

The finding that bradyzoite occupancy within tissue cysts can be highly varied (Fig. 3B; see Fig. S2B in the supplemental material) prompted us to develop a strategy to allow for comparative analysis to provide insights into the patterns of bradyzoite growth *in vivo*. Toward this end, we introduce the notion of packing density, which is a measure of the bradyzoite burden relative to the volume of the tissue cyst housing the bradyzoites (Fig. 4 and 5). This metric allows for the direct comparison of tissue cysts normalized to the variability associated with tissue cyst size at all time points of harvest (Fig. 2C). The observation that tissue cysts of the same volume can contain vastly different bradyzoite burdens (Fig. 3B) establishes that bradyzoite growth cannot be the primary driver of cyst size (Fig. 4A). Rather, the data suggest that tissue cyst expansion in general outpaces bradyzoite replication (Fig. 4C and 5A), resulting in a lowering of the packing density with size. However, cyst expansion may serve as a signal for bradyzoite replication, resulting in an increase in the packing density within a given cyst (Fig. 4B). This likely contributes to the differences in the packing densities of tissue cysts that are exactly the same size (Fig. 5A). Thus, a complex pattern apparently involving alternating episodes of tissue cyst expansion and bradyzoite replication appears to govern the development of bradyzoites within tissue cysts.

In all of these studies, we are limited to imaging tissue cysts that are harvested at the various time points. We therefore rely on snapshots from which patterns of growth must be inferred. True longitudinal studies following the fate of a tissue cyst over weeks, though theoretically possible using multiphoton imaging and cra-

nial windows (79), present daunting technical challenges, rendering them not feasible at this time.

Evidence for sporadic endodyogeny within tissue cysts has been reported in several morphological studies at the electron microscopic level (12, 43). We confirm that replication of parasites within cysts does occur by endodyogeny, having captured key intermediates in the process, including the formation of daughter buds, expansion and segregation of the nucleus during mitosis, and the progression of cytokinesis using TgIMC3 as a marker (Fig. 6; see Fig. S3 in the supplemental material). We further confirm that the parasites undergoing replication are in fact true bradyzoites based on their labeling with TgSRS9 and the absence of TgSAG1 labeling (Fig. 8; Fig. S5 and S6). This pattern was largely maintained in tissue cysts harvested at all time points between weeks 3 and 8 (Fig. 8).

TgIMC3 has proven to be the ideal target to investigate the dynamics of bradyzoite replication within tissue cysts purified from infected-mouse brains. Not only does this protein exhibit differential intensity in daughter parasites versus the mother (Fig. 6, 7, and 9; see Fig. S3 to Fig. S7 in the supplemental material), but it is also reported to progressively decay in its labeling with time after "birth" (56, 58) (Fig. 9). Several reports, primarily studies of cell culture, have reported that the switch from tachyzoites to bradyzoites is associated with both a reduction in replicative capacity and the loss of replicative synchrony (15, 16, 23, 39). These studies have led to the assumption that bradyzoite replication *in vivo* must occur in a sporadic and asynchronous fashion (39, 42). Our findings, based on the detection of replication intermediates using TgIMC3 staining, find evidence for sporadic and isolated replication (one or two bradyzoites replicating within a tissue cyst optical section) and clustered replication (Fig. 7), which by definition is asynchronous within the cyst as a whole. What is evident in these instances is that not only is the intensity of TgIMC3 higher where replication is occurring but the size and density of nuclei are also higher, suggestive of recent doubling (Fig. 7). What we did not expect to find in our analysis on replication patterns was evidence for highly synchronized replication whereby every parasite within the cyst was replicating simultaneously or all parasites within a cyst demonstrated a prior synchronized replicative event, resulting in a uniform TgIMC3 labeling intensity (Fig. 7). Synchronous replication is viewed as a trait of actively growing tachyzoites but not bradyzoites (55). The frequency of synchronous replication was highest early in the chronic phase, suggestive of relative temporal closeness to their tachyzoite origins. However, synchronous replication was also observed to spike at week 6 (data not shown) and week 8 postinfection (Fig. 7), well into the chronic phase. The regulatory control required to coordinate entry into the cell cycle and progression through it for hundreds of bradyzoites within a tissue cyst suggests a complex regulatory landscape that likely has an epigenetic basis and involves some significant degree of bradyzoite-to-bradyzoite communication. The mechanistic basis for such coordination is not known, although evidence for "social behavior" in protozoa has been documented in well-developed systems like *Dictyostelium discoideum* (80, 81) and trypanosomatids (82–84). In addition, bradyzoite replication within tissue cysts could also be initiated by the ability of parasites to sense their neighbors (or the cyst wall) or their absence by means of contact inhibition.

Given that each tissue cyst owes its origins to a single tachyzoite leaves open the possibility that inherently coded developmental

decisions defined potentially by an epigenetic basis (36–38) contribute to both synchronous and clustered replication within tissue cysts *in vivo*. Finally, recent evidence pointing to the drift in stochastic processes evolving toward directed outputs in biological systems, including replication timing (85), could additionally serve as a basis for what present as highly coordinated behaviors (86–88).

The spatial organization of replication within cysts, as seen with clusters of replicating parasites (Fig. 7), could also suggest functional compartmentalization within a tissue cyst that may govern nutrient availability. Such a system may underlie some of the rare patterns of replication observed within cysts, including the "ring of replication" at the periphery of the cysts or other "waves of replication" (see Fig. S4 in the supplemental material) that are observed. In addition, clusters of replicating parasites could be the consequence of prior localized bradyzoite death providing a nutrient source as other parasites cannibalize them, as has been previously suggested (12, 43). Most likely, however, no one mechanism is likely to regulate the spatial organization of replication within tissue cysts *in vivo*.

The capacity to directly count bradyzoite numbers within cysts using BradyCount 1.0 (Fig. 3A), which reveals a trend of increasing bradyzoite numbers over the course of the chronic phase (Fig. 3C), and the potential for alternating cycles of tissue cyst expansion and bradyzoite replication (Fig. 5B) are both suggestive of temporal regulation. The use of TgIMC3 intensity as a marker for the recency of replication (Fig. 9) provides a unifying point of reference to begin to establish insights into the patterns of bradyzoite growth during the chronic phase. Consistent with their proximity to their tachyzoite origins, tissue cysts at week 3 exhibited both the highest levels of mean TgIMC3 intensity for the whole cyst and the broadest range of intensities (Fig. 9B and C). In contrast, tissue cysts harvested at week 5 exhibited uniformly lower mean TgIMC3 intensities, indicative of a considerably longer time point between the last replicative event and harvest (Fig. 9B). While it would be tempting to suggest that no replication occurred between weeks 3 and 5, the data from the mean bradyzoite burden at this time point does not support this contention (Fig. 3C). This suggests that TgIMC3 intensity likely decays in a time frame shorter than 2 weeks. Future studies examining intermediate time points will help establish a more precise time frame with the development of specific cell cycle markers to monitor progression *in vivo* (A. Dhara and A. P. Sinai, unpublished data). The finding that the mean TgIMC3 signal in tissue cysts harvested at week 8 (Fig. 9B and C) were between those at week 3 and 5 confirms that significant replication did occur between weeks 5 and 8. Given the apparent decay kinetics for TgIMC3, the present data cannot distinguish between a pattern of additive asynchronous growth and an episode of growth and harvest during the waning phase of the TgIMC3 intensity profile (Fig. 9D). We provisionally favor the former scenario, as the brightest cysts exhibit evidence for asynchronous replication based on the TgIMC3 pattern (Fig. 9C).

TgIMC3 yields information on the timing of replication, but not the unlinked expansion of the tissue cyst. We therefore plotted the TgIMC3 intensity profiles for week 3, 5, and 8 tissue cysts relative to both the cyst diameter (Fig. 10A) and the packing density (Fig. 10B). Notably, tissue cyst size did not correlate in any way with the TgIMC3 intensity at either week 3 or week 5, although the size of tissue cysts expanded (Fig. 10A). In contrast, cysts harvested at week 8 reveal that small and intermediate sized cysts were more likely to contain more recently replicating bradyzoites (Fig. 10A), while the mean diameter of the cysts increases relative to those at week 5 (Fig. 10A). Likewise, no specific pattern emerges when comparing the relationship between TgIMC3 intensity and packing density (a metric that integrates bradyzoite burden with cyst size). This is not surprising at week 3, as most parasites are within recently formed cysts where recent replication (as a tachyzoite) balances the absence of a time interval for significant expansion as a cyst (Fig. 10B). In contrast, the corollary appears to be responsible at week 5 where tissue cyst expansion is occurring but relatively little by way of recent bradyzoite replication (Fig. 10B). Consequently, the overall pattern for the distribution of the packing densities relative to TgIMC3 intensity at weeks 3 and 5 are very similar, as illustrated by the trapezoids outlining the dot plots (Fig. 10B).

In contrast, consistent with enhanced replication between weeks 5 and 8 (Fig. 9B), a positive correlation is observed between TgIMC3 intensity and packing density (Fig. 10B), indicating that the most recent replicative events (higher TgIMC3 intensity) tend to be in more densely packed cysts. When viewed in the context of the size distribution of the week 8 tissue cysts (Fig. 10A and Table 1), the increasing packing density reveals that parasite replication most likely occurs within the most "hollow" cysts, consistent with tissue cyst expansion needed to precede replicative events.

Although we can examine only "snapshots" of tissue cysts, the combination of TgIMC3 intensity and packing density provide a mechanism to begin to understand the growth dynamics of bradyzoites within cysts and to develop computational approaches to model these complex growth patterns (A. Patwardhan and A. P. Sinai, unpublished data). Such models when viewed in the context of drug treatments and changes in immune/physiological status *in vivo* will provide for the first time insights into how bradyzoites develop within tissue cysts, opening up new areas of investigation and drug development.

The studies presented in this article force us to reexamine our view of bradyzoites and the tissue cysts that house them. On the basis of the body of data presented, we propose a framework within which bradyzoite development can be examined *in vivo* (Fig. 11). At the heart of this framework is the fact that tissue cysts and the bradyzoites within them are nonuniform with regard to their replicative capacity and physiology. All bradyzoites within the host develop from tachyzoites that possess a high replicative capacity and as a consequence elevated TgIMC3 labeling. In response to immune pressure and other stressors, increased replicative asynchrony accompanies the development of the tissue cyst, now enclosed in the cyst wall (Fig. 11). These "transitional bradyzoites" express bradyzoite markers and downregulate tachyzoite markers but are not that far removed from their tachyzoite origins. One might speculate that bradyzoites closest to their tachyzoite origins are more likely to reactivate having to overcome a lower developmental barrier. As bradyzoites mature, reduced replicative capacity may reduce the likelihood of spontaneous reactivation, thereby resulting in a cyst that possesses an "intermediate" phenotype with a mixed population containing both more recently replicating parasites and parasites that have not replicated for an extended time period (based on TgIMC3 intensity). These heterogenous tissue cysts would be predicted to be most versatile containing populations of bradyzoites capable of rapid reactivation to tachyzoites while others drift toward a more entrenched dormancy that could be primed for transmission to the next host
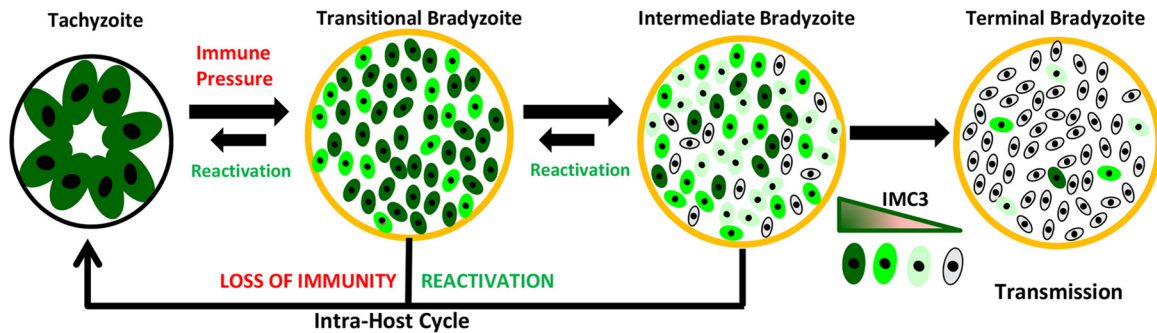
**FIG 11** Development of bradyzoites within tissue cysts *in vivo*. All tissue cysts arise from tachyzoites where the high growth rate and synchrony in replication account for a high mean TgIMC3 intensity. Immune pressure contributes to stage conversion noted by the development of the tissue cyst wall (orange). The early transitional bradyzoites exhibit reduced growth rate (noted by the variability in TgIMC3 intensity) relative to tachyzoites while still retaining the capacity for significant replication with a high degree of synchrony within the tissue cyst. The proposed intermediate bradyzoites within a tissue cyst exhibit greater asynchrony in replication depicted by a greater range of TgIMC3 intensities. We hypothesize that the retained replicative potential of both the transitional and intermediate bradyzoite populations contributes to a lower threshold for reactivation. Accordingly, these cysts possess the highest likelihood of both spontaneous reactivation and reactivation in the context of immune suppression. Finally, we hypothesize that progression toward deeper dormancy resulting in the terminal bradyzoite-possessing cysts may have a lower threshold for reactivation within the host but are geared for transmission to the next host. The heterogeneity of replication patterns would still permit a low level of sporadic replication within these terminal tissue cysts. Together, we propose that tissue cysts, while genetically clonal, are physiologically and phenotypically varied with regard to the bradyzoites they house.

in the act of carnivory. The truly long-term persistent cysts are predicted to enter a state of deep dormancy, defining what we refer to as a terminal bradyzoite. In this state, bradyzoites are not likely to reactivate within the host but are predicted to be primed for efficient transmission.

Our work further expands the repertoire of activities revealed in the heterogeneity of bradyzoite responses inherent in the patterns of growth. This suggests higher orders of regulation whereby bradyzoites within a tissue cyst are either genetically programmed to be heterogenous or achieve this status spontaneously. This heterogeneity in replication may extend to overall changes in the physiological state such that any given tissue cyst is optimally tuned to have subpopulations of organisms geared toward specific hosts, thereby hedging one's bets, ensuring that transmission is successful regardless of the host. As a clonal entity, successful transmission of any single bradyzoite ensures success for the cyst as a whole. Finally, the development of approaches to directly assess actual bradyzoite burdens for the first time focuses the study of the chronic phase onto the organisms rather than the population of parasites that define the tissue cyst. This increase in resolution will promote more expansive mechanistic studies on this critical life cycle stage.

## MATERIALS AND METHODS

***Toxoplasma* and mouse infection.** The *T. gondii* type II strain ME49 was used exclusively in this study. Parasites were maintained by serially passaging 18 to 20 tissue cysts of infected-mouse brains homogenized in cold phosphate-buffered saline (PBS) with 0.3% Tween 80 (final concentration). Details regarding the homogenization of infected-mouse brains are found in Text S1 in the supplemental material. Female 4- to 6-week-old CBA/J mice obtained from Jackson Laboratories (Bar Harbor, ME) were typically infected following a week-long acclimatization and no later than 3 weeks following delivery. Mice were monitored daily for the development of symptoms associated with acute toxoplasmosis. The attrition rate during the acute phase was less than 5% over the roughly 2-year course of this study. Tissue cyst harvests were performed during the course of the chronic phase between weeks 3 and 8 postinfection as indicated. Animals were provided standard chow and water *ad libitum*. In instances where animals appeared symptomatic, either a veterinarian-approved dough or

gel diet was provided on the cage floor. Severely ill animals were euthanized. Euthanasia of animals used for the harvesting of tissue cysts was performed by $CO_2$ asphyxiation, followed by cervical dislocation, in accordance with the approved protocols. All protocols associated with the care, treatment, and infection of mice were approved by the University of Kentucky IACUC.

**Tissue cyst purification.** The purification of tissue cysts was achieved by a modified version of the protocol of Cornellison et al. employing a discontinuous Percoll gradient (41). In contrast to the Cornellison protocol where the brain homogenate is layered onto a discontinuous two-step gradient comprised on a 90%/30% Percoll gradient (in PBS) (Sigma, St. Louis, MO), we developed a three-step system in which 9 ml of 90% Percoll is overlaid with 4.5 ml each of 40% and 20% Percoll. This modification permits the resolution of tissue cysts based on their density. Gradients were set up in 50-ml conical tubes (Falcon; Becton-Dickinson, Franklin Lakes, NJ) and layered with the homogenate of at most two infected-mouse brains. The gradients were centrifuged at 2,200 rpm for 18 min using a high brake setting in a Beckman Allegra table top centrifuge with a swinging bucket rotor. The time was set when the centrifuge came up to speed. The harvesting of the gradients was achieved by the insertion of a glass capillary to the bottom of the tube connected to a peristaltic pump calibrated to a flow rate of 2 ml/min using double-distilled water ($ddH_2O$). The entire gradient was collected into Eppendorf tubes with roughly 1 ml per fraction. The enumeration of tissue cysts was achieved by transferring 10 $\mu$l of each fraction into a well of a 96-well plate containing 100 $\mu$l of PBS. Tissue cysts were deposited onto the surface of the well by spinning the plate at 2,000 rpm for 5 min. Only fractions 10 and higher were counted, as tissue cysts were never observed in fractions 1 to 9 (data not shown). Once the tissue cysts in a given well were directly counted using an inverted microscope with a 10× or 20× objective (Nikon), the value was multiplied by 100 to obtain the total number of cysts in the fraction. As all of the cyst preparations reported were generated from the brains of two infected mice, the mean cyst burden was defined as the sum of the cysts across all fractions divided by 2. A detailed description of all steps in the purification of tissue cysts is presented in Text S1 in the supplemental material.

**Antibodies and immunofluorescence microscopy.** The following previously described antibodies and reagents were used at the indicated concentrations. All antibodies and reagents were diluted into PBS supplemented with 1 mM $CaCl_2$ and 1 mM $MgCl_2$ (PBS++) with 3% bovine serum albumin (BSA) and 1× Carbo-Block (Vector Laboratories, Burlin-

game, CA). The following antibodies were used: rabbit anti-TgSAG1 (1:3,000) (30) and rabbit anti-TgSRS9 (1:1,000) (27) provided by John Boothroyd, Stanford University; rat anti-TgIMC3 (1:1,000) (56) provided by Marc-Jan Gubbels, Boston College; and rhodamine-conjugated *Dolichos biflorus* agglutinin (DBA) lectin (1:2,000) (Vector Laboratories). Hoechst 33342 (5 $\mu$g/ml) (Molecular Probes/Invitrogen) was used. Detection of antibodies was achieved using highly cross-adsorbed species-specific fluorescently conjugated secondary antibodies (Invitrogen) at a dilution of 1:2,000.

Percoll fractions containing tissue cysts were diluted at least 1:10 in PBS and pelleted to remove the Percoll. The cyst pellet was gently resuspended in PBS to a concentration of between 200 and 400 cysts per ml. Tissue cysts were spun onto glass slides using a Cytospin centrifuge (Shandon Cytospin 4) at 750 rpm for 5 min with medium acceleration and brake. These conditions resulted in minimal damage to tissue cysts, as higher speeds caused widespread breakage, while lower speed/acceleration profiles resulted in disruption due to shear forces on the cyst wall (data not shown). The slides were fixed by immersion into a slide staining jar containing methanol ($-20°C$). Slides were stored at $-20°C$ until they were labeled for the indirect immunofluorescence assay (IFA).

Slides to be stained were transferred to PBS++ (PBS with 1 mM CaCl$_2$ and 1 mM MgCl$_2$) and brought to room temperature. Staining of slides was achieved by making a barrier using a wax pencil around the spot where the tissue cysts were deposited. The appropriate labeling solution was placed directly on the deposited cysts in the space encircled with the wax pencil for 45 min to an hour. The primary labeling mix was aspirated, and the slides were washed three times with PBS++ in a Coplin jar. Secondary antibodies were added as described above for the primary antibodies. The labeled tissue cysts were covered with Mowiol for imaging, and then a coverslip was placed over the cysts.

**Imaging of tissue cysts.** All microscopy presented was performed using a Zeiss Axioplan stand equipped with fluorescence capability and a motorized z-stage. Tissue cysts were initially identified based on either DBA or Hoechst staining using a 40×/0.8-numerical-aperture (NA) oil immersion objective. Images of individual cysts were recorded using a 100×/1.4NA PlanApo objective. Following the setting of exposure levels for the Hoechst (DNA), fluorescein isothiocyanate (FITC), and rhodamine/Texas Red channels, a z-stack comprised of eight optical slices was acquired using the Hoechst (DNA) signal to define the "poles" of the tissue cyst. Eight optical sections were acquired for all cysts regardless of their diameter. Images were acquired for each of the channels sequentially within a z-stack using a Zeiss AxioCam MRM camera in the linear acquisition mode. The black-and-white images were pseudocolored. Where relevant, the z-stacks were imported into the AxioVision deconvolution suite and subjected to image processing using the iterative algorithm. Final images were cropped in Adobe Photoshop, and any manipulation of brightness and contrast was applied uniformly to the image. Finally, for each imaged tissue cyst, we also acquired a Nomarski (differential interference contrast [DIC]) illumination image. The diameters of all imaged tissue cysts (defined by the widest z-stack) were established using the linear measurement tool in the AxioVision software suite that was calibrated using a stage micrometer.

**Imaging tissue cysts in brain sections.** An intact brain freshly harvested from an infected mouse was fixed for a minimum of 3 days in a fixative comprised of (vol/vol) 10% formalin, 70% ethanol (EtOH), and 5% acetic acid. The entire brain was sliced into 30-$\mu$m sections, and the sections were transferred in pools into the wells of 24-well plates containing cryoprotectant and stored at $-20°C$. Individual sections were transferred into 2 ml of cold PBS++ and washed three times for 10 min in the cold. The section was transferred to a fresh 24-well plate stained with DBA lectin (1:6,000) and Hoechst (1:2,000) in 3% BSA in PBS++. The plate was incubated at 4°C with gentle rocking in the cold overnight. The sections were then washed in PBS++ as described above and spread out on a glass slide prior to being covered with Mowiol and a coverslip. Tissue cysts were identified as DBA halos using both 40× and 100× objectives.

The presence of the tissue cysts was confirmed using the distinctive nuclear pattern (Hoechst stain) as well as DIC imaging.

**Development of BradyCount 1.0.** The BradyCount 1.0 imaging software was developed to directly enumerate the bradyzoite burden within tissue cysts based on the direct quantification of nuclear profiles. Images of z-sections of tissue cysts were acquired in RGB (red-green-blue) with 24-bit resolution, with virtually all of the information related to nuclei present in a single (blue) channel (see Fig. S9 in the supplemental material). Therefore, the original image was converted to an 8-bit grayscale image. The grayscale image can be considered to be constituted of three distinct parts: (i) the dark background, outside the tissue cyst; (ii) bright spots defining the nuclei; and (iii) the intermediate gray areas within the cyst (Fig. S9). The pixel histogram shows that the gray values of the dark area are narrow (the field is uniformly dark), while the bright spots (nuclei) and surrounding gray areas exhibit a wide range of pixel distributions (Fig. S9). We therefore used top hat and bottom hat filters to enhance the peaks (bright signal/nuclei) and suppress the lows (dark regions), establishing an intensity range to which a nonlinear transform was used to utilize the full range of resolution (0 to 255 pixels).

Once filtered images were transformed to exploit the full pixel range, the grayscale image was converted into a binary image by using a modified Otsu threshold algorithm (89). This algorithm assumes that the image can be thresholded to contain two classes of pixels (foreground [bright] and background [dark]). The algorithm then calculates the optimum threshold separating these two classes so as to minimize interclass variance resulting in a binary converted image (see Fig. S9 in the supplemental material). Once the image is converted to a binary form, two options were considered to localize and subsequently count the parasite nuclei. In the first approach, we compute the distance transform of the binary image and then set a threshold regarding regions above the threshold as seed for the watershed segmentation algorithm (90). Following the watershed segmentation, the area of the nuclei is segmented into small regions where each region represents a nucleus. Each such region contains multiple pixels which are in effect connected components. These computed components are conceptually splitting the image into horizontal runs of adjacent pixels, each with a unique label. This process is rerun by using the horizontal labels in the vertical plane. Subsequent merging of the directional labels define the discrete entities that are generated equals the number of regions which also equals the number of nuclei and by extension bradyzoites. The second option, which was not selected to process the imaging data, involves the repetitive iterative adjustment of both the grayscale and Otsu threshold values until the individual nuclei are discretely outlined using a Laplacian or Gaussian operator to detect their edges. This approach requires user supervision, resulting in more variability based on the operator using the program (data not shown). For this reason, we selected the first approach for BradyCount 1.0.

**Establishment of the bradyzoite burden and packing density.** The Hoechst (DNA) image used to establish the diameter of a tissue cyst was opened in the BradyCount 1.0 software. The thresholding function was used to simultaneously outline individual nuclear profiles in the imported DNA image and the adjacent program-generated mask. Once individual nuclear profiles are clearly demarcated to the satisfaction of the user, clicking the "count" function on the program window generates the number of nuclei within the given optical section. This value, $N$, represents the number of nuclei and by extension bradyzoite number in the imaged optical section. The packing density (PD) represents the number of parasites per unit imaged volume defined by the volume of the imaged cylinder. This volume is determined by the area of the cross section ($\pi r^2$ [where $r$ is the radius]) × diameter/8, as each z-stack had eight optical sections (see Fig. S3A in the supplemental material). The PD was plotted relative to cyst volume (diameter), time of harvest, and TgIMC3 intensity to provide new insights into the developmental patterns of bradyzoites within tissue cysts.

**Quantitation of TgIMC3 intensity.** Tissue cysts harvested at various time points (weeks 3, 5, and 8) postinfection were stained at the same time

with the same aliquot of anti-TgIMC3 antibody (in addition to DBA and Hoechst). Both an initial static tissue cyst image (for TgIMC3) and a subsequent z-stack were acquired (for all channels). The exposure time for all the static TgIMC3 images was set at 780 ms. The raw TgIMC3 images were uploaded into NIH ImageJ, and the entire cyst was outlined as the region of interest. By clicking "measure," the total pixel intensity normalized to the area of the tissue cyst was established. The DBA and Hoechst images were used to determine the diameter and number of nuclei (bradyzoites), respectively, that were used to establish the relationships between TgIMC3 intensity and both cyst diameter (volume) and the packing density.

**Statistical analysis.** All the graphs and relevant statistical tests used in the work were generated by GraphPad Prism version 6.00 (La Jolla, CA, USA). In light of the data sets possessing different numbers of data points and a broad distribution of values compiled from multiple independent experiments, we selected analysis of variance (ANOVA) to establish differences based on the time of cyst harvest. These data sets included the tissue cyst burden, tissue cyst diameter, number of nuclei (bradyzoites) within tissue cysts, and TgIMC3 signal intensity. The $P$ value was determined by Brown-Forsythe test and corrected Bartlett's test (corrected for any deviation from Gaussian distribution). The difference between any two group means (for the specific test metric) was analyzed using Tukey's multiple-comparison tests with a 95% confidence interval. See specific figure legends for the values of the test statistic and the significance level. Additionally, a box plot analysis was done to demonstrate how an apparently static population (no significant change based on one-way ANOVA analysis) changed when considering the mean number of nuclei (bradyzoites) and the packing density over time. These changes are reflected by the shifts in the respective median values and the distribution ranges (see Fig. S2B and S2D in the supplemental material).

## SUPPLEMENTAL MATERIAL

Supplemental material for this article may be found at http://mbio.asm.org/lookup/suppl/doi:10.1128/mBio.01155-15/-/DCSupplemental.

Text S1, DOCX file, 1 MB.
Figure S1, PDF file, 0.1 MB.
Figure S2, PDF file, 0.1 MB.
Figure S3, PDF file, 0.4 MB.
Figure S4, PDF file, 0.2 MB.
Figure S5, PDF file, 0.3 MB.
Figure S6, PDF file, 0.5 MB.
Figure S7, PDF file, 0.4 MB.
Figure S8, PDF file, 0.1 MB.
Figure S9, PDF file, 0.1 MB.

## ACKNOWLEDGMENTS

## REFERENCES

1. **Dubey JP**. 1998. Advances in the life cycle of Toxoplasma gondii. Int J Parasitol **28**:1019–1024. http://dx.doi.org/10.1016/S0020-7519(98)00023-X.
2. **Hill D, Dubey JP**. 2002. Toxoplasma gondii: transmission, diagnosis and prevention. Clin Microbiol Infect **8**:634–640. http://dx.doi.org/10.1046/j.1469-0691.2002.00485.x.
3. **Dubey JP, Lindsay DS, Speer CA**. 1998. Structures of Toxoplasma gondii tachyzoites, bradyzoites, and sporozoites and biology and development of tissue cysts. Clin Microbiol Rev **11**:267–299.
4. **Dubey JP, Jones JL**. 2008. Toxoplasma gondii infection in humans and animals in the United States. Int J Parasitol **38**:1257–1278. http://dx.doi.org/10.1016/j.ijpara.2008.03.007.
5. **Chew WK, Wah MJ, Ambu S, Segarra I**. 2012. Toxoplasma gondii: determination of the onset of chronic infection in mice and the *in vitro* reactivation of brain cysts. Exp Parasitol **130**:22–25. http://dx.doi.org/10.1016/j.exppara.2011.10.004.
6. **Takashima Y, Suzuki K, Xuan X, Nishikawa Y, Unno A, Kitoh K**. 2008. Detection of the initial site of Toxoplasma gondii reactivation in brain tissue. Int J Parasitol **38**:601–607. http://dx.doi.org/10.1016/j.ijpara.2007.09.017.
7. **Israelski DM, Chmiel JS, Poggensee L, Phair JP, Remington JS**. 1993. Prevalence of Toxoplasma infection in a cohort of homosexual men at risk of AIDS and toxoplasmic encephalitis. J Acquir Immune Defic Syndr **6**:414–418.
8. **Nath A, Sinai AP**. 2003. Cerebral toxoplasmosis. Curr Treat Options Neurol **5**:3–12. http://dx.doi.org/10.1007/s11940-003-0018-8.
9. **Tenter AM, Heckeroth AR, Weiss LM**. 2000. Toxoplasma gondii: from animals to humans. Int J Parasitol **30**:1217–1258. http://dx.doi.org/10.1016/S0020-7519(00)00124-7.
10. **Ferguson DJ**. 2004. Use of molecular and ultrastructural markers to evaluate stage conversion of Toxoplasma gondii in both the intermediate and definitive host. Int J Parasitol **34**:347–360. http://dx.doi.org/10.1016/j.ijpara.2003.11.024.
11. **Ferguson DJ, Graham DI, Hutchison WM**. 1991. Pathological changes in the brains of mice infected with Toxoplasma gondii: a histological, immunocytochemical and ultrastructural study. Int J Exp Pathol **72**:463–474.
12. **Ferguson DJ, Hutchison WM**. 1987. An ultrastructural study of the early development and tissue cyst formation of Toxoplasma gondii in the brains of mice. Parasitol Res **73**:483–491. http://dx.doi.org/10.1007/BF00535321.
13. **Fortier B, Coignard-Chatain C, Soete M, Dubremetz JF**. 1996. Structure and biology of Toxoplasma gondii bradyzoites. C R Seances Soc Biol Fil **190**:385–394. (In French.)
14. **Sims TA, Hay J, Talbot IC**. 1990. Ultrastructural immunocytochemistry of the intact tissue cyst of Toxoplasma in the brains of mice with congenital toxoplasmosis. Ann Trop Med Parasitol **84**:141–147.
15. **Dzierszinski F, Nishi M, Ouko L, Roos DS**. 2004. Dynamics of Toxoplasma gondii differentiation. Eukaryot Cell **3**:992–1003. http://dx.doi.org/10.1128/EC.3.4.992-1003.2004.
16. **Singh U, Brewer JL, Boothroyd JC**. 2002. Genetic analysis of tachyzoite to bradyzoite differentiation mutants in Toxoplasma gondii reveals a hierarchy of gene induction. Mol Microbiol **44**:721–733. http://dx.doi.org/10.1046/j.1365-2958.2002.02903.x.
17. **White MW, Radke JR, Radke JB**. 2014. Toxoplasma development-turn the switch on or off? Cell Microbiol **16**:466–472 http://dx.doi.org/10.1111/cmi.12267.
18. **Tomita T, Bzik DJ, Ma YF, Fox BA, Markillie LM, Taylor RC, Kim K, Weiss LM**. 2013. The Toxoplasma gondii cyst wall protein CST1 is critical for cyst wall integrity and promotes bradyzoite persistence. PLoS Pathog **9**:e1003823. http://dx.doi.org/10.1371/journal.ppat.1003823.
19. **Lane A, Soete M, Dubremetz JF, Smith JE**. 1996. Toxoplasma gondii: appearance of specific markers during the development of tissue cysts *in vitro*. Parasitol Res **82**:340–346. http://dx.doi.org/10.1007/s004360050123.
20. **Martin AM, Liu T, Lynn BC, Sinai AP**. 2007. The Toxoplasma gondii parasitophorous vacuole membrane: transactions across the border. J Eukaryot Microbiol **54**:25–28. http://dx.doi.org/10.1111/j.1550-7408.2006.00230.x.
21. **Lemgruber L, Lupetti P, Martins-Duarte ES, De Souza W, Vommaro RC**. 2011. The organization of the wall filaments and characterization of the matrix structures of Toxoplasma gondii cyst form. Cell Microbiol **13**:1920–1932. http://dx.doi.org/10.1111/j.1462-5822.2011.01681.x.
22. **Radke JB, Lucas O, De Silva EK, Ma Y, Sullivan WJ, Jr, Weiss LM, Llinas M, White MW**. 2013. ApiAP2 transcription factor restricts development of the Toxoplasma tissue cyst. Proc Natl Acad Sci U S A **110**:6871–6876. http://dx.doi.org/10.1073/pnas.1300059110.
23. **Sullivan WJ, Jr, Jeffers V**. 2012. Mechanisms of Toxoplasma gondii persistence and latency. FEMS Microbiol Rev **36**:717–733. http://dx.doi.org/10.1111/j.1574-6976.2011.00305.x.
24. **Weiss LM, Kim K**. 2000. The development and biology of bradyzoites of Toxoplasma gondii. Front Biosci **5**:D391–D405. http://dx.doi.org/10.2741/Weiss.
25. **de Carvalho L, Souto-Padrón T, de Souza W**. 1991. Localization of lectin-binding sites and sugar-binding proteins in tachyzoites of Toxoplasma gondii. J Parasitol **77**:156–161. http://dx.doi.org/10.2307/3282574.

26. **Sethi KK, Rahman A, Pelster B, Brandis H**. 1977. Search for the presence of lectin-binding sites on Toxoplasma gondii. J Parasitol **63:**1076–1080. http://dx.doi.org/10.2307/3279850.

27. **Kim SK, Karasov A, Boothroyd JC**. 2007. Bradyzoite-specific surface antigen SRS9 plays a role in maintaining Toxoplasma gondii persistence in the brain and in host control of parasite replication in the intestine. Infect Immun **75:**1626–1634. http://dx.doi.org/10.1128/IAI.01862-06.

28. **Van TT, Kim SK, Camps M, Boothroyd JC, Knoll LJ**. 2007. The BSR4 protein is up-regulated in Toxoplasma gondii bradyzoites, however the dominant surface antigen recognised by the P36 monoclonal antibody is SRS9. Int J Parasitol **37:**877–885. http://dx.doi.org/10.1016/j.ijpara.2007.02.001.

29. **Zhang YW, Kim K, Ma YF, Wittner M, Tanowitz HB, Weiss LM**. 1999. Disruption of the Toxoplasma gondii bradyzoite-specific gene BAG1 decreases in vivo cyst formation. Mol Microbiol **31:**691–701. http://dx.doi.org/10.1046/j.1365-2958.1999.01210.x.

30. **Kim SK, Boothroyd JC**. 2005. Stage-specific expression of surface antigens by Toxoplasma gondii as a mechanism to facilitate parasite persistence. J Immunol **174:**8038–8048. http://dx.doi.org/10.4049/jimmunol.174.12.8038.

31. **Al-Anouti F, Tomavo S, Parmley S, Ananvoranich S**. 2004. The expression of lactate dehydrogenase is important for the cell cycle of Toxoplasma gondii. J Biol Chem **279:**52300–52311. http://dx.doi.org/10.1074/jbc.M409175200.

32. **Lunghi M, Galizi R, Magini A, Carruthers VB, Di Cristina M**. 2015. Expression of the glycolytic enzymes enolase and lactate dehydrogenase during the early phase of Toxoplasma differentiation is regulated by an intron retention mechanism. Mol Microbiol **96:**1159–1175. http://dx.doi.org/10.1111/mmi.12999.

33. **Dzierszinski F, Mortuaire M, Dendouga N, Popescu O, Tomavo S**. 2001. Differential expression of two plant-like enolases with distinct enzymatic and antigenic properties during stage conversion of the protozoan parasite Toxoplasma gondii. J Mol Biol **309:**1017–1027. http://dx.doi.org/10.1006/jmbi.2001.4730.

34. **Ferguson DJ, Parmley SF, Tomavo S**. 2002. Evidence for nuclear localisation of two stage-specific isoenzymes of enolase in Toxoplasma gondii correlates with active parasite replication. Int J Parasitol **32:**1399–1410. http://dx.doi.org/10.1016/S0020-7519(02)00129-7.

35. **Pittman KJ, Aliota MT, Knoll LJ**. 2014. Dual transcriptional profiling of mice and Toxoplasma gondii during acute and chronic infection. BMC Genomics **15:**806. http://dx.doi.org/10.1186/1471-2164-15-806.

36. **Behnke MS, Radke JB, Smith AT, Sullivan WJ, Jr, White MW**. 2008. The transcription of bradyzoite genes in Toxoplasma gondii is controlled by autonomous promoter elements. Mol Microbiol **68:**1502–1518. http://dx.doi.org/10.1111/j.1365-2958.2008.06249.x.

37. **Nardelli SC, Che FY, Silmon de Monerri NC, Xiao H, Nieves E, Madrid-Aliste C, Angel SO, Sullivan WJ, Jr, Angeletti RH, Kim K, Weiss LM**. 2013. The histone code of Toxoplasma gondii comprises conserved and unique posttranslational modifications. mBio **4**(6):e00922-13. http://dx.doi.org/10.1128/mBio.00922-13.

38. **Sullivan WJ, Jr, Smith AT, Joyce BR**. 2009. Understanding mechanisms and the role of differentiation in pathogenesis of Toxoplasma gondii: a review. Mem Inst Oswaldo Cruz **104:**155–161. http://dx.doi.org/10.1590/S0074-02762009000200005.

39. **Knoll LJ, Tomita T, Weiss LM**. 2014. Bradyzoite development, p 521–549. *In* Weiss LM, Kim K (ed), Toxoplasma gondii. The model apicomplexan: perspectives and methods, 2nd ed. Elsevier, London, United Kingdom.

40. **Manger ID, Hehl A, Parmley S, Sibley LD, Marra M, Hillier L, Waterston R, Boothroyd JC**. 1998. Expressed sequence tag analysis of the bradyzoite stage of Toxoplasma gondii: identification of developmentally regulated genes. Infect Immun **66:**1632–1637.

41. **Cornelissen AW, Overdulve JP, Hoenderboom JM**. 1981. Separation of Isospora (Toxoplasma) gondii cysts and cystozoites from mouse brain tissue by continuous density-gradient centrifugation. Parasitology **83:**103–108. http://dx.doi.org/10.1017/S0031182000050071.

42. **Sullivan AM, Zhao X, Suzuki Y, Ochiai E, Crutcher S, Gilchrist MA**. 2013. Evidence for finely regulated asynchronous growth of Toxoplasma gondii cysts based on data-driven model selection. PLoS Comput Biol **9:**e1003283. http://dx.doi.org/10.1371/journal.pcbi.1003283.

43. **Ferguson DJ, Huskinson-Mark J, Araujo FG, Remington JS**. 1994. A morphological study of chronic cerebral toxoplasmosis in mice: compar-

44. ison of four different strains of Toxoplasma gondii. Parasitol Res **80:**493–501. http://dx.doi.org/10.1007/BF00932696.

44. **Ferguson DJ, Hutchison WM**. 1987. The host-parasite relationship of Toxoplasma gondii in the brains of chronically infected mice. Virchows Arch A Pathol Anat Histopathol **411:**39–43. http://dx.doi.org/10.1007/BF00734512.

45. **Ferguson DJ, Hutchison WM, Pettersen E**. 1989. Tissue cyst rupture in mice chronically infected with Toxoplasma gondii. An immunocytochemical and ultrastructural study. Parasitol Res **75:**599–603. http://dx.doi.org/10.1007/BF00930955.

46. **Weiss LM, Laplace D, Takvorian PM, Tanowitz HB, Cali A, Wittner M**. 1995. A cell culture system for study of the development of Toxoplasma gondii bradyzoites. J Eukaryot Microbiol **42:**150–157. http://dx.doi.org/10.1111/j.1550-7408.1995.tb01556.x.

47. **Knoll LJ, Boothroyd JC**. 1998. Molecular biology's lessons about Toxoplasma development: stage-specific homologs. Parasitol Today **14:**490–493. http://dx.doi.org/10.1016/S0169-4758(98)01347-7.

48. **Hooshyar H, Rostamkhani P, Arbabi M**. 2009. Study on growth of Toxoplasma gondii tissue cyst in laboratory mouse. Jundishpur J Microbiol **2:**140–143.

49. **Sinai AP**. 2008. Biogenesis of and activities at the Toxoplasma gondii parasitophorous vacuole membrane. Subcell Biochem **47:**155–164.

50. **Sinai AP, Paul S, Rabinovitch M, Kaplan G, Joiner KA**. 2000. Coinfection of fibroblasts with Coxiella burnetti and Toxoplasma gondii: to each their own. Microbes Infect **2:**727–736. http://dx.doi.org/10.1016/S1286-4579(00)90362-9.

51. **Sinai AP, Webster P, Joiner KA**. 1997. Association of host cell endoplasmic reticulum and mitochondria with the Toxoplasma gondii parasitophorous vacuole membrane: a high affinity interaction. J Cell Sci **110:**2117–2128.

52. **Ferguson DJ, Huskinson-Mark J, Araujo FG, Remington JS**. 1994. An ultrastructural study of the effect of treatment with atovaquone in brains of mice chronically infected with the ME49 strain of Toxoplasma gondii. Int J Exp Pathol **75:**111–116.

53. **Francia ME, Striepen B**. 2014. Cell division in apicomplexan parasites. Nat Rev Microbiol **12:**125–136. http://dx.doi.org/10.1038/nrmicro3184.

54. **Behnke MS, Wootton JC, Lehmann MM, Radke JB, Lucas O, Nawas J, Sibley LD, White MW**. 2010. Coordinated progression through two subtranscriptomes underlies the tachyzoite cycle of Toxoplasma gondii. PLoS One **5:**e12354. http://dx.doi.org/10.1371/journal.pone.0012354.

55. **Gubbels MJ, White M, Szatanek T**. 2008. The cell cycle and Toxoplasma gondii cell division: tightly knit or loosely stitched? Int J Parasitol **38:**1343–1358. http://dx.doi.org/10.1016/j.ijpara.2008.06.004.

56. **Anderson-White BR, Ivey FD, Cheng K, Szatanek T, Lorestani A, Beckers CJ, Ferguson DJ, Sahoo N, Gubbels MJ**. 2011. A family of intermediate filament-like proteins is sequentially assembled into the cytoskeleton of Toxoplasma gondii. Cell Microbiol **13:**18–31. http://dx.doi.org/10.1111/j.1462-5822.2010.01514.x.

57. **Radke JR, Striepen B, Guerini MN, Jerome ME, Roos DS, White MW**. 2001. Defining the cell cycle for the tachyzoite stage of Toxoplasma gondii. Mol Biochem Parasitol **115:**165–175. http://dx.doi.org/10.1016/S0166-6851(01)00284-5.

58. **Anderson-White B, Beck JR, Chen CT, Meissner M, Bradley PJ, Gubbels MJ**. 2012. Cytoskeleton assembly in Toxoplasma gondii cell division. Int Rev Cell Mol Biol **298:**1–31. http://dx.doi.org/10.1016/B978-0-12-394309-5.00001-8.

59. **Doggett JS, Nilsen A, Forquer I, Wegmann KW, Jones-Brando L, Yolken RH, Bordón C, Charman SA, Katneni K, Schultz T, Burrows JN, Hinrichs DJ, Meunier B, Carruthers VB, Riscoe MK**. 2012. Endochin-like quinolones are highly efficacious against acute and latent experimental toxoplasmosis. Proc Natl Acad Sci U S A **109:**15936–15941. http://dx.doi.org/10.1073/pnas.1208069109.

60. **Matuschka FR**. 1977. The effect of sulfomethoxypyrazine-pyrimethamine therapy on the fine structure of Toxoplasma gondii-cysts in the brain of Mastomys natalensis. Scanning and transmission electron microscopical investigations. Zentralbl Bakteriol Orig A **238:**419–429.

61. **Werner H, Matuschka FR, Brandenburg I**. 1979. Structural changes of Toxoplasma gondii bradyzoites and cysts following therapy with sulfamethoxypyrazine-pyrimethamine: studies by light and electron microscopy. Consequences for chemotherapy. Zentralbl Bakteriol Orig A **245:**240–253.

62. **Gormley PD, Pavesio CE, Minnasian D, Lightman S**. 1998. Effects of

drug therapy on Toxoplasma cysts in an animal model of acute and chronic disease. Invest Ophthalmol Vis Sci **39:**1171–1175.

63. **Chew WK, Segarra I, Ambu S, Mak JW.** 2012. Significant reduction of brain cysts caused by Toxoplasma gondii after treatment with spiramycin coadministered with metronidazole in a mouse model of chronic toxoplasmosis. Antimicrob Agents Chemother **56:**1762–1768. http://dx.doi.org/10.1128/AAC.05183-11.

64. **Hester J, Mullins J, Sa Q, Payne L, Mercier C, Cesbron-Delauw MF, Suzuki Y.** 2012. Toxoplasma gondii antigens recognized by IgG antibodies differ between mice with and without active proliferation of tachyzoites in the brain during the chronic stage of infection. Infect Immun **80:**3611–3620. http://dx.doi.org/10.1128/IAI.00604-12.

65. **Suzuki Y, Wang X, Jortner BS, Payne L, Ni Y, Michie SA, Xu B, Kudo T, Perkins S.** 2010. Removal of Toxoplasma gondii cysts from the brain by perforin-mediated activity of CD8+ T cells. Am J Pathol **176:**1607–1613. http://dx.doi.org/10.2353/ajpath.2010.090825.

66. **Gazzinelli R, Xu Y, Hieny S, Cheever A, Sher A.** 1992. Simultaneous depletion of CD4+ and CD8+ T lymphocytes is required to reactivate chronic infection with Toxoplasma gondii. J Immunol **149:**175–180.

67. **Odaert H, Soête M, Fortier B, Camus D, Dubremetz JF.** 1996. Stage conversion of Toxoplasma gondii in mouse brain during infection and immunodepression. Parasitol Res **82:**28–31. http://dx.doi.org/10.1007/BF03035408.

68. **Nance JP, Vannella KM, Worth D, David C, Carter D, Noor S, Hubeau C, Fitz L, Lane TE, Wynn TA, Wilson EH.** 2012. Chitinase dependent control of protozoan cyst burden in the brain. PLoS Pathog **8:**e1002990. http://dx.doi.org/10.1371/journal.ppat.1002990.

69. **Kamerkar S, Davis PH.** 2012. Toxoplasma on the brain: understanding host-pathogen interactions in chronic CNS infection. J Parasitol Res **2012:**589295. http://dx.doi.org/10.1155/2012/589295.

70. **Carruthers VB, Suzuki Y.** 2007. Effects of Toxoplasma gondii infection on the brain. Schizophr Bull **33:**745–751. http://dx.doi.org/10.1093/schbul/sbm008.

71. **Blanchard N, Dunay IR, Schlüter D.** 2015. Persistence of Toxoplasma gondii in the central nervous system: a fine-tuned balance between the parasite, the brain and the immune system. Parasite Immunol **37:**150–158. http://dx.doi.org/10.1111/pim.12173.

72. **Resende MG, Fux B, Caetano BC, Mendes EA, Silva NM, Ferreira AM, Melo MN, Vitor RW, Gazzinelli RT.** 2008. The role of MHC haplotypes H2d/H2b in mouse resistance/susceptibility to cyst formation is influenced by the lineage of infective Toxoplasma gondii strain. An Acad Bras Cienc **80:**85–99. http://dx.doi.org/10.1590/S0001-37652008000100005.

73. **Lee YH, Kasper LH.** 2004. Immune responses of different mouse strains after challenge with equivalent lethal doses of Toxoplasma gondii. Parasite **11:**89–97. http://dx.doi.org/10.1051/parasite/200411189.

74. **Suresh K, Mak JW, Yong HS.** 1991. Immune response in acute Toxoplasma infection of Balb/C, ICR and CBA/J mice. Southeast Asian J Trop Med Public Health **22:**452–454.

75. **Koshy AA, Cabral CM.** 2014. 3-D imaging and analysis of neurons infected in vivo with Toxoplasma gondii. J Vis Exp **2014:**e52237. http://dx.doi.org/10.3791/52237.

76. **Vyas A.** 2015. Mechanisms of host behavioral change in Toxoplasma gondii rodent association. PLoS Pathog **11:**e1004935. http://dx.doi.org/10.1371/journal.ppat.1004935.

77. **Sutterland AL, Fond G, Kuin A, Koeter MW, Lutter R, van Gool T, Yolken R, Szoke A, Leboyer M, de Haan L.** 2015. Beyond the association. Toxoplasma gondii in schizophrenia, bipolar disorder, and addiction: systematic review and meta-analysis. Acta Psychiatr Scand **132:**161–179 http://dx.doi.org/10.1111/acps.12423.

78. **Torrey EF, Bartko JJ, Yolken RH.** 2012. Toxoplasma gondii and other risk factors for schizophrenia: an update. Schizophr Bull **38:**642–647. http://dx.doi.org/10.1093/schbul/sbs043.

79. **Ricard C, Debarbieux FC.** 2014. Six-color intravital two-photon imaging of brain tumors and their dynamic microenvironment. Front Cell Neurosci **8:**57. http://dx.doi.org/10.3389/fncel.2014.00057.

80. **Gomer RH, Jang W, Brazill D.** 2011. Cell density sensing and size determination. Dev Growth Differ **53:**482–494. http://dx.doi.org/10.1111/j.1440-169X.2010.01248.x.

81. **Loomis WF.** 2014. Cell signaling during development of Dictyostelium. Dev Biol **391:**1–16. http://dx.doi.org/10.1016/j.ydbio.2014.04.001.

82. **Lopez MA, Nguyen HT, Oberholzer M, Hill KL.** 2011. Social parasites. Curr Opin Microbiol **14:**642–648. http://dx.doi.org/10.1016/j.mib.2011.09.012.

83. **Lopez MA, Saada EA, Hill KL.** 2015. Insect stage-specific adenylate cyclases regulate social motility in African trypanosomes. Eukaryot Cell **14:**104–112. http://dx.doi.org/10.1128/EC.00217-14.

84. **Oberholzer M, Saada EA, Hill KL.** 2015. Cyclic AMP regulates social behavior in African trypanosomes. mBio **6**(3):e01954-14. http://dx.doi.org/10.1128/mBio.01954-14.

85. **Bechhoefer J, Rhind N.** 2012. Replication timing and its emergence from stochastic processes. Trends Genet **28:**374–381. http://dx.doi.org/10.1016/j.tig.2012.03.011.

86. **Goldbeter A, Gérard C, Gonze D, Leloup JC, Dupont G.** 2012. Systems biology of cellular rhythms. FEBS Lett **586:**2955–2965. http://dx.doi.org/10.1016/j.febslet.2012.07.041.

87. **Meyer HM, Roeder AH.** 2014. Stochasticity in plant cellular growth and patterning. Front Plant Sci **5:**420. http://dx.doi.org/10.3389/fpls.2014.00420.

88. **Székely T, Jr, Burrage K.** 2014. Stochastic simulation in systems biology. Comput Struct Biotechnol J **12:**14–25. http://dx.doi.org/10.1016/j.csbj.2014.10.003.

89. **Otsu N.** 1979. A threshold selection method from gray-level histograms. IEEE Trans Syst Man Cybern **9:**62–66. http://dx.doi.org/10.1109/TSMC.1979.4310076.

90. **Roerdink JBTM.** 2000. The watershed transform: definitions, algorithms and parallelization strategies. Fundamenta Informaticae **41:**127–228.